

N° d'ordre : 3301

THESE

En vue de l'obtention du : **DOCTORAT**

Structure de Recherche : **Equipe de Physique des Hautes Energies-Modélisation et Simulation**

Discipline : **Physique**

Spécialité : **Physique Médicale**

Présentée et soutenue le **07/03/2020** par :

Youssef BOUZEKRAOUI

OPTIMIZATION OF SPECT IMAGING SIMULATION, IN NUCLEAR MEDICINE USING MONTE CARLO CALCULATION

JURY

El Hassan SAIDI,	PES, Faculté des Sciences, Université Mohammed V - Rabat	Président
Mohammed AGGOUR,	PES, Faculté des Sciences, Université Ibn Tofail - Kénitra	Rapporteur / Examineur
Mohammed CHERRAJ,	PH, Faculté des Sciences, Université Mohammed V - Rabat	Rapporteur / Examineur
Farida BENTAYEB,	PES, Faculté des Sciences, Université Mohammed V - Rabat	Directeur de thèse
Rachid AHL LAAMARA,	PH, Faculté des Sciences, Université Mohammed V - Rabat	Rapporteur / Examineur

Année Universitaire : 2019-2020

Acknowledgements

I am deeply thankful to God, by the grace of whom the progress and success of this work was possible.

The work presented in this thesis was carried out in the High Energy Physics, Modeling and Simulation Laboratory (LPHE-MS) of the physics department of the Faculty of Sciences of Rabat.

This work is done in the frame by the International Atomic Energy Agency "Doctoral CRP in Advances in Medical imaging Techniques. I would express my grateful thanks the (IAEA) for their support and interest.

This work could not have been done without the agreement, support and help of many people.

First and foremost, I would like to express grateful thanks to my supervisor Farida BENTAYEB Professor of Higher Education at the Faculty of Sciences, Rabat, for her invaluable help, her ideas, her patience and perseverance in monitoring my work and her invaluable advice and also for always being there to encourage me, to support me, and to have allowed me to continue trust and leave me the necessary freedom to carry out my work. supervision and valuable reviewing of this thesis.

I extend my sincere thanks to Mr El Hassan SAIDI, Professor of Higher Education at the Faculty of Sciences, Rabat, who did me the honor of accepting the presidency of the jury. Please accept, Sir, the assurance of my deep respect.

Also, I would like to thank Professor Mr Mohammed CHERRAJ for having done me the honor of having come to my defense. I'm extremely grateful to him for the interest he has shown in this research work by committing to be a reporter and for agreeing to judge this work as an examiner. May he find here the testimony of my heartfelt thanks.

I would like to thank Mr Mohammed AGGOUR, Professor at the Kenitra Faculty of Science, for the interest he has shown in this research work by committing to be a reporter and for agreeing to judge this work as an examiner. Let him find here the expression of my deep consideration.

A big thank to Mr Rachid AHL LAAMARA, Professor at the Faculty of Sciences, Rabat, who was kind enough to be a reporter and for agreeing to judge this work as an examiner. Please accept, Sir, the assurance of my deep respect.

Finally I would express my grateful thanks for my parents for the help and encouragement during the whole life.

Résumé

Le choix du radionucléide a un rôle clé en médecine nucléaire qui apparaît comme la fraction de dispersion la plus faible. Le choix de la fenêtre d'énergie d'acquisition n'est pas trivial, du fait de la répartition énergétique continue et étendue des photons de Freinage (Bremsstrahlung). De plus, la présence de photons pénétrés et dispersés provenant du collimateur dans les images de tomographie par émission de photons uniques dégrade la résolution et le contraste. Ainsi, la qualité de l'image dépend de la sensibilité et de la résolution du système détecteur-collimateur. L'objectif de ce travail consistait tout d'abord à utiliser une étape différente du code de simulation SIMIND MC pour comparer la qualité d'image pouvant être obtenue avec trois radionucléides : technétium-99 m (Tc-99 m), iode-123 (I-123) et samarium-153 (Sm-153). En imagerie de tomographie par émission monophotonique (SPECT) en yttrium-90 (Y-90), nous étudions les effets des fenêtres d'énergie sur le rapport de contraste de l'image sur l'image (CNR), afin de sélectionner la fenêtre d'énergie optimale pour l'imagerie Y-90. Et pour déterminer les fenêtres principale et secondaire d'énergie pour la méthode de correction de dispersion de fenêtre à triple énergie (TEW) à l'aide du code de simulation SIMIND Monte Carlo en imagerie Gadolinium-159 (Gd-159). Les résultats montrent que Tc-99 m et Sm-153 donnent les meilleurs résultats, avec un collimateur LEHR pour la résolution spatiale, alors que, avec le collimateur ME, donne une résolution inférieure à la résolution I-123, la fenêtre d'énergie optimale obtenue pour l'imagerie SPECT Y-90 bremsstrahlung était [120–150] keV, et les fenêtres d'énergie optimales pour la scintigraphie au Gd-159 étaient les fenêtres d'énergie secondaire de 3 et 6 keV. Ces résultats pourraient être utiles pour la quantification de l'imagerie Gd-159.

Mots-clés: Freinage, CNR, Fantôme Jaszczak, SIMIND, Imagerie par tomodensitométrie à émission de photons simples d'yttrium-90, Rapports de diffusion au total, Sensibilité, Résolution spatiale.

Summary

The choice of the radionuclide has a key role in nuclear medicine which appearing the lowest scatter fraction. the choice of the acquisition energy window is not trivial, due to the continuous and broad energy distribution of the bremsstrahlung photons. In addition, the presence of penetrated and scattered photons from collimator in single photon emission computed tomography images degrade resolution and contrast. Thus, image quality depends on sensitivity and resolution of the collimator–detector system. The objective of this work was firstly how to use a different step of SIMIND MC Simulation Code, to compare the image quality that can be achieved by three radionuclides: technetium 99 m (Tc-99m), iodine-123 (I-123), and samarium-153 (Sm-153), In yttrium 90 (Y-90) single photon emission computed tomography (SPECT) imaging, we investigate the effects of the energy windows on the image contrast to noise ratio (CNR), in order to select the optimal energy window for Y-90 imaging. And to determine the main and sub-energy windows for triple energy window (TEW) scatter correction method using the SIMIND Monte Carlo simulation code in Gadolinium-159 (Gd-159) imaging. The results show that Tc-99m and Sm-153 give best and results with LEHR collimator for spatial resolution, whereas, I-123 provided with ME collimator a lower resolution, also the optimal energy window obtained for Y-90 bremsstrahlung SPECT imaging was [120–150] keV, and the optimal energy windows for Gd-159 scintigraphy were the sub energy windows of 3 and 6 keV. These findings could be helpful in the quantification of Gd-159 imaging.

Keywords: Bremsstrahlung, CNR, Jaszczak phantom, SIMIND, yttrium 90 single photon emission computed tomography imaging, Scatter to Total Ratios, sensitivity, spatial resolution,

Résumé détaillé

L'imagerie nucléaire est la technique d'examen standard pour évaluer la fonction physiologique. Elle consiste à déterminer la distribution dans l'organisme d'une substance radioactive administrée au patient, dite radiotraceur, en détectant le rayonnement qu'elle émet au moyen d'un dispositif de détection adapté au rayonnement externe. Le choix du radionucléide a un rôle clé en médecine nucléaire qui semble être la fraction de diffusion la plus faible. De plus, la présence de photons pénétrés et diffusés provenant du collimateur dans les images de tomographie calculée par émission de photons uniques dégrade la résolution et le contraste. Ainsi, la qualité de l'image dépend de la sensibilité et de la résolution du système collimateur-détecteur. Il existe deux modes d'imagerie par émission: le premier est la tomodensitométrie à émission de photons uniques (SPECT), dans laquelle le radiotraceur émet des photons de type gamma qui sont détectés par une caméra gamma. La crédibilité de la quantification des images obtenues se heurte cependant à divers obstacles liés aux limites de performance des détecteurs (en termes de résolution spatiale, de résolution énergétique et de sensibilité de détection): par les effets physiques, tels que l'atténuation et la diffusion, et par des effets physiologiques (mouvements du patient et effets liés à la reconstruction tomographique), entraînant des distorsions dans la formation de l'image et même un faux diagnostic. Les effets doivent donc être corrigés par des méthodes de correction spécifiques afin d'extraire des paramètres quantitatifs fiables. Malgré l'évolution de la technologie médicale qui se manifeste par l'apparition et la rénovation continue de nouvelles méthodes de diagnostic, plusieurs problèmes liés à la distribution et à l'atténuation demeurent. La modélisation des processus de formation d'image semble difficile en présence d'effets parasites. Les simulations de Monte-Carlo s'avèrent être un outil très puissant pour une telle modélisation. Ces simulations contribuent à la conception et à l'optimisation des détecteurs, mais aussi à la modélisation réaliste des phénomènes physiques intervenant lors d'un examen de médecine nucléaire. L'inconvénient majeur des simulations Monte-Carlo est le temps de calcul important qu'elles nécessitent. De nombreux simulateurs sont actuellement disponibles, mais aucun d'entre eux ne s'est encore imposé comme un standard en imagerie nucléaire, car chacun a ses spécificités et ses défauts. La présence du collimateur est également une grave pénalité en termes de résolution spatiale et de sensibilité. D'autres limites technologiques sont dues aux phénomènes physiques d'atténuation, de diffusion, de variation de la résolution spatiale de la caméra et du bruit de mesure. L'origine physique et la description de ces phénomènes sont fournies et leurs effets sur la qualité et la quantification des images sont soulignés. C'est essentiellement une dégradation de la résolution spatiale et un contraste des sections reconstruites qui conduisent à des erreurs de quantification des images en artefacts, et affectent l'estimation de dimensions et de concentrations fiables. Les simulations numériques sont utilisées dans différents domaines scientifiques car elles permettent de reproduire par calcul un phénomène physique dont le comportement décrit par un système d'équations mathématiques doit être évalué. Ils produisent des données très proches de la réalité et fournissent ainsi

des solutions approximatives à des problèmes complexes qui sont même coûteux à résoudre avec une approche expérimentale. Leur exploitation dans le domaine de l'imagerie médicale a considérablement augmenté ces dernières années pour étudier et développer de nouveaux dispositifs d'imagerie virtuelle. Il existe deux principaux types de simulations numériques: les méthodes déterministes qui résolvent le problème analytiquement à partir d'un ensemble d'équations de modèle et les méthodes probabilistes utilisant des simulations de Monte Carlo. Les méthodes analytiques consistent à modéliser un phénomène physique à partir d'un système d'équations avec autant de relations que de paramètres inconnus. Ainsi, le suivi des particules est modélisé à partir des équations qui décrivent leur transport dans la matière. L'inconvénient de ces méthodes est que seul le faisceau primaire est modélisé, les photons diffusés ne peuvent pas être considérés. Ils conduisent donc à des résultats théoriques qui, dans certains cas, ne correspondent pas à la réalité et donc manquent de précision. Néanmoins, ils restent réalisables et efficaces pour les petits calculs. Les simulations de Monte Carlo sont intéressantes pour modéliser des configurations trop compliquées pour une simulation analytique. Dans l'imagerie Y-90 bremsstrahlung, la qualité et la quantification de l'image sont limitées en raison des niveaux élevés de diffusion d'objets, de pénétration septale du collimateur et de diffusion du collimateur. Le collimateur de trous parallèles et l'optimisation de la fenêtre d'énergie dans Y-90 ont été étudiés. Dans cette étude, nous avons utilisé le code SIMIND de simulation de Monte Carlo pour démontrer comment la qualité d'image se dégrade en fonction des paramètres d'imagerie. Nous avons évalué la qualité de l'image en tenant compte du contraste et du rapport contraste / bruit (CNR). Les données de simulation indiquent que le choix de la fenêtre d'énergie d'acquisition pour l'imagerie Y-90 a un grand effet sur le contraste de l'image et le rapport contraste / bruit. Les valeurs de contraste élevées dans le centre de 135 keV pour les deux acquisitions. On remarque que les meilleures valeurs CNR sont obtenues dans les trois premières fenêtres. Les simulations montrent également que la pénétration est un problème important pour le collimateur HE à HE. Le collimateur HE avec une fenêtre d'énergie entre 120 et 150 keV a été sélectionné comme paramètre d'acquisition optimal en tenant compte du contraste et du rapport contraste / bruit (CNR) et des photons géométriques, de pénétration et de diffusion. L'optimisation du collimateur et de la fenêtre d'énergie d'acquisition permet d'améliorer la précision quantitative et la qualité d'image du SPECT Y-90 bremsstrahlung. Le gadolinium-159 en tant qu'émetteur bêta est un radionucléide efficace pour le traitement du cancer. La prise en charge thérapeutique nécessite une imagerie quantitative, difficile à réaliser en raison de plusieurs facteurs, tels que la dispersion des objets. Des études antérieures sur les propriétés des images thérapeutiques et scintigraphiques avec Gd-159 ont démontré que les images obtenues avec un collimateur polyvalent à haute énergie possédaient une faible qualité. Les méthodes de correction de dispersion sont utiles pour améliorer la qualité d'image et la quantification de l'activité. évalué et comparé six méthodes de correction de diffusion pour le spectre SPECT Tc-99m en utilisant la simulation SIMIND Monte Carlo. Ils ont introduit la méthode TEW, considérant l'approximation triangulaire, comme la procédure de correction la plus appropriée. Cependant, il n'y a pas d'étude concernant la fraction des photons diffusés Gd-159 en fonction des fenêtres optimales principale et sous-énergétique pour la mise en œuvre de la méthode TEW. La sélection des fenêtres principales et sous-énergétiques optimales est très importante et peut conduire à une qualité d'image appropriée. Par conséquent, la sélection des fenêtres principale et sous-énergétique était différente dans l'imagerie SPECT Gd-159. Il est important de choisir les fenêtres d'énergie appropriées pour éviter les photons diffusés qui dégradent la quantification et la qualité de l'image. En conséquence, les fenêtres

principales et sous-énergétiques choisies imposent un grand effet sur la correction de la dispersion pour l'imagerie SPECT Gd-159. Le Tc-99m et le Sm-153 offrent les meilleures propriétés d'imagerie généralement similaires avec LEHR. Pour I-123, le collimateur ME aide à réduire l'influence des rayons gamma à haute énergie.

List of Abbreviations

CNR	Contrast to Noise Ratio
CERN	European Center for Nuclear Research
DEW	Dual-Energy Window
EGS	Electron Gamma Shower
FWHM	Full Width at Half Maximum
FWTM	Full Width at Ten Maximum
GATE	Geant4 Application for Emission Tomography
GEANT	GEometry ANd Tracking
Gd-159	Gadolinium-159
HE	High Energy
I-123	Iodine-123
LEHR	Low Energy High Resolution
ME	Midium Energy
MCNPX	Monte Carlo N-Particle eXtended
MCNP	Monte Carlo N-particle Transport Code
MLEM	Maximum Likelihood Expectation-Maximization
MRI	Magnitic Resonanc Imagings
OSEM	Ordered Subsets Expectation Maximization
P/T	Primary to Total
PET	Positron Emission Tomography
PSF	Point Spread Function
SIMIND	SIMulation of Imaging Nuclear Detectors
Sm-153	Samarium- 153
SPECT	Single Photon Emission Computed Tomography
Tc-99	Technetium-99
TEW	Triple Energy Window
Y-90	Yttrium-90

Contents

Résumé	2
Summary	3
Résumé détaillé	4
Introduction	14
1 Literature Review and Theoretical Aspect	16
1.1 Introduction	16
1.2 The activities of nuclear medicine	16
1.2.1 Diagnostic acts "IN VITRO"	16
1.2.2 Diagnostic acts "IN VIVO"	16
1.2.3 Therapeutic acts	17
1.3 Emission Tomography in Nuclear Medicine	17
1.4 Radiation	17
1.4.1 Non-Ionizing radiation	18
1.4.2 Ionizing radiation	18
1.5 Medical Uses of Radiation	18
1.5.1 Radiotherapy	18
1.5.2 Medical Imaging	18
1.6 Radioisotopes in Medicine	19
1.6.1 Radioisotopes production for nuclear medicine	19
1.6.2 Radiopharmaceutical	19
1.6.3 Radiopharmaceutical Characteristics	20
1.6.4 Physical properties of Yttrium-90	20
1.6.5 Technetium-99m	21
1.7 Gamma Camera	22
1.7.1 The detection head	22
1.7.2 Collimator	23
1.7.3 The scintillating crystal	24
1.7.4 The light guide	24
1.7.5 The analog circuit	25
1.7.6 Processors	26
1.7.7 Acquisition of data	27
1.7.8 Online corrections	27
1.7.9 Data processing	28

1.7.10	Types of acquisition	28
1.8	Performance of a gamma-camera: Evaluation and Potential improvements	29
1.8.1	Performance of a gamma-camera: Evaluation	30
1.8.2	Sensitivity	32
1.8.3	Spatial linearity	32
1.8.4	Uniformity	32
1.8.5	The Image Quality in Nuclear Medicine	32
1.8.6	Contrast	33
1.8.7	Factors Affecting Image Contrast [77]	33
1.8.8	Noise	34
1.9	Limits of SPECT imaging	36
1.9.1	Physiological factors	36
1.9.2	Physical factors	36
1.9.3	Attenuation	37
1.9.4	Noise measurement	39
1.10	Conclusion	39
2	Monte carlo simulation	40
2.1	Introduction	40
2.2	Monte Carlo simulations	41
2.2.1	Principle of the Monte Carlo method	41
2.2.2	Inversion method	41
2.2.3	Rejection method	42
2.2.4	Application of Monte Carlo methods	42
2.3	Generic codes	44
2.4	The dedicated codes	45
2.5	Simind	46
2.6	SPECT tomographic reconstruction methods	48
2.6.1	Principle	48
2.6.2	Analytical Methods: Filtered Projection (RPF) Back Projection	49
2.6.3	Iterative methods	49
2.7	Methods for correcting scintigraphic images	49
2.7.1	Correction of attenuations	49
2.7.2	Fixed resolution loss with depth	50
2.7.3	Elimination of photons in acquired projections	50
2.7.4	Triple energy window	51
2.7.5	Movement of the patient	52
2.7.6	Conclusion	52
3	Contributions of the Monte Carlo study for optimization of medical imaging	53
3.1	Contrast optimization for Y-90 SPECT imaging	53
3.1.1	Introduction	53
3.1.2	Materials and Methods	54
3.1.3	Results	55
3.2	Determination of the Energy Windows for the TEW Scatter Correction Method in Gd-159 SPECT Using Monte Carlo Simulation	58

3.2.1	Introduction	58
3.2.2	Materials and Methods	58
3.2.3	Results	60
3.3	Comparison of image quality of different radionuclides Tc-99m, Sm-153, and I-123	62
3.3.1	Introduction	62
3.3.2	Materials and Methods	62
3.3.3	Results and Discussion	64
3.4	Conclusion	67
	Conclusion	68
	Bibliography	69

List of Figures

1.1	Decay pattern of strontium-90 to yttrium-90, to zirconium-90[16]	20
1.2	The different components of the detection head[24]	23
1.3	A descriptive diagram of a hexagonal collimator [24]	23
1.4	The different types of collimator[24]	24
1.5	Diagram of a gamma-camera of Anger [24]	26
1.6	Principle of calculating the position of the interaction point in the crystal[24]	27
1.7	Parameters of a parallel collimator	31
1.8	Pulse-height spectra recorded with a NaI(Tl) detector for different γ -ray energies	34
1.9	Comparative pulse-height spectra recorded from a ^{99m}Tc source with NaI(Tl) and Ge(Li) detectors	35
1.10	Planar (upper left) and single-photon emission computed tomographic (SPECT) (center) images of a thoracic phantom	36
1.11	Photoelectric effect	38
1.12	Compton scattering	38
2.1	The different stages of the Monte Carlo simulation	43
2.2	The coordinate system for simind program	46
2.3	Simind program operation mode	47
2.4	virtual Phantom MDP	47
2.5	image obtained after the tomographic reconstruction	48
2.6	Reconstruction of an object with multiple structures	49
2.7	spatial resolution of the source - detector distance	50
2.8	Principle of the triple subtraction method	51
3.1	Monte Carlo simulated spectrum for yttrium-90[105]	55
3.2	Contributions of geometric, penetration, scatter, and X-rays components with energy windows[105]	56
3.3	Contrast of the six spheres with energy window	56
3.4	Images of simulated Jaszczak phantom with a high-energy collimator using large energy windows (above) and narrow energy windows (below)	57
3.5	CNR of the six spheres	57
3.6	Geometry of the single photon emission computed tomography system and phantom	59
3.7	Gadolinium-159 point sources obtained for the sub-windows of 3 keV and a main energy window of 10%	61
3.8	Energy spectra of photons on the detector without the use of collimator[101]	64

3.9	Planar images created at the end of each simulation	65
3.10	Point spread function for technetium-99 m, Samarium-153, and Iodine-123 . . .	65
3.11	Sensitivity at the end of simulation[104]	66

List of Tables

1.1	properties of the main scintillators used in nuclear medicine)	25
3.1	Collimator specifications	54
3.2	Size and central position for the sub-windows of the large window-set	54
3.3	Size and central position for the sub-windows of the narrow window-set	54
3.4	Characteristics of the Siemens Symbia medical system collimator	59
3.5	Difference between the true primary to total ratio (%) and primary to total ratio estimated by triple-energy window scatter correction method for sub-window 3	60
3.6	Difference between the true primary to total ratio (%) and primary to total ratio estimated by triple-energy window scatter correction method for sub-window 6[106]	60
3.7	Collimator specifications	63
3.8	Energies and intensities of gamma rays emitted from: The technetium-99m, samarium-153, and iodine-123 sources	63
3.9	Geometric, penetration, and scatter fractions achieved with the isotopes	64
3.10	Full width at half maximum, full width at tenth maximum, and sensitivity data for the different radionuclides point source[104]	66

Introduction

Nuclear imaging is the standard examination technique for assessing physiological function. It consists in determining the distribution in the body of a radioactive substance administered to the patient, known as radiotracer, by detecting the radiation that it emits by means of a detection device adapted to external radiation. The choice of radionuclide has a key role in nuclear medicine which appears to be the lowest scatter fraction. In addition, the presence of penetrated and scattered photons from collimator in single photon emission computed tomography images degrade resolution and contrast. Thus, image quality depends on sensitivity and resolution of the collimator–detector system. There are two modes of emission imaging: the first is single photon emission computed tomography (SPECT), in which the radiotracer emits gamma-type photons that are detected by a gamma camera. The second is Positron Emission Tomography (PET), for which the radiotracer emits positrons and the two gamma photons emitted in coincidence are detected after annihilation of the positron with an electron. The data acquired by the detectors are processed using a tomographic reconstruction algorithm to estimate the three-dimensional distribution of the radiotracer in the body. Nuclear imaging provides non-invasive access to information about the functioning of organs and to study physiological and metabolic processes that other imaging techniques do not allow. The credibility of the quantification of the images obtained, however, faces various obstacles related to the limits of the performance of the detectors (in terms of spatial resolution, energy resolution and detection sensitivity): by the physical effects, such as attenuation and diffusion, and by physiological effects (movements of the patient and effects related to tomographic reconstruction), resulting in distortions in the formation of the image and even a false diagnosis. The effects must therefore be corrected by specific correction methods in order to extract reliable quantitative parameters. Despite the evolution of medical technology that is manifested by the appearance and continued renovation of new diagnostic methods, several problems related to the distribution and mitigation remain. The modeling of the processes of image formation seems difficult in the presence of parasitic effects. Monte-Carlo simulations prove to be a very powerful tool for such modeling. These simulations help in the design and optimization of the detectors, but also to the realistic modeling of the physical phenomena taking place during a nuclear medicine examination. The major disadvantage of Monte-Carlo simulations is the large computation time they require. Many simulators are currently available, but none of them has yet established itself as a standard in nuclear imaging, because each has its own specificities and its own shortcomings. To achieve the objectives of our work, we proceeded in the following way:

The first chapter introduces the basic concepts of nuclear medicine, their fields and their applications, as well as the principles of SPECT, the detection device, the acquisition modes and the a gamma camera performance and the limitations of emission imaging pertaining rather to physiological factors.

Chapter II presents the Monte Carlo simulation principles (random number generation, sam-

pling, etc.) and the simulation platform SIMIND and ImageJ. The tomographic reconstruction and the main reconstruction algorithms used in SPECT are then illustrated. In this chapter the correction methods developed to correct image-degrading phenomena and preventing precise and reliable quantification of reconstructed sections (attenuation, scattering, variability of the detector's response function) are also presented.

In chapter III, present a contribution of simulation Monte Carlo in Medical Imaging, the main and sub-energy windows for triple energy window (TEW) scatter correction method are determined, using the SIMIND Monte Carlo simulation code in Gadolinium-159 (Gd-159) imaging, the energy effects on the image quality are developed in order to select the optimal energy window for Y-90 imaging, finally a comparison study of the image quality that can be achieved by three radionuclides, namely technetium 99m (Tc-99m), iodine 123 (I-123), and samarium 153 (Sm-153); In the end of this work, a general conclusion displaying the different results and findings was showed.

Chapter 1

Literature Review and Theoretical Aspect

1.1 Introduction

Nuclear medicine includes the biological and medical uses of artificial radionuclides in unsealed sources. This field is based on distinct activities: functional imaging (scintigraphy), metabolic therapy and biological assay (radioimmunoassay). In imaging, nuclear medicine is also complementary to other techniques using ionizing radioisotopes (radiology, tomodesitometry, etc.) or non-ionizing radiation (ultrasound, nuclear magnetic resonance imaging, etc.). Since the 1950s, the applications of nuclear medicine have undergone a great progress. They are featured by the ability to detect with a very high sensitivity the radiation emitted by the radioactive atoms, isotopes chosen for their metabolism and / or physio-pathological properties. As the radioelement is introduced by the venous way in the body of a patient. The alone product or associated to a vector with a predetermined tropism of an organ or pathology, is followed by external detection and gives the possibility to record its distribution, concentration and elimination, by an appropriate detection system, called "gamma camera". We will list next the various activities of nuclear medicine and radioelements selected.

1.2 The activities of nuclear medicine

1.2.1 Diagnostic acts "IN VITRO"

These acts are based on the use of labeled reagents. They do not require the administration of a radiopharmaceutical to the patient. Radioimmunological techniques make it possible to easily assay many substances of biological interest (hormones, vitamins, enzymes, drugs, tumor antigens) which cannot be obtained by conventional techniques, because of the complexity of their structure or the weakness of their properties. (their content in biological media) [1].

1.2.2 Diagnostic acts "IN VIVO"

These actions require that the radiopharmaceutical be received by the patient. These diagnoses permit the determination of the fraction of the administered activity fixed by an organ and the biological samples radioactivity (blood, urine, stool, etc.) in order to measure different parameters (blood volume, duration of erythrocytes, etc.) and to study the distribution in the body of

the radiopharmaceutical administered with radiographic and tomoscintigraphic techniques. It can either simply transit through the body or attach itself to an organ [2]. The main purpose of scintigraphy is not to provide morphological information of generally inferior quality to that provided by other imaging techniques (conventional radiology, computed tomography, ultrasound or magnetic resonance imaging), but information about the functional value of an organ as well as the presence of tumor or inflammatory lesions.

1.2.3 Therapeutic acts

They use isotopes that are essentially emitters of particles or radiation which are enough energetic to treat certain cancers or to attenuate them, but which are also used in non-cancerous pathologies such as hyperthyroidism (e.g. iodine) 131). [1].

1.3 Emission Tomography in Nuclear Medicine

Emission tomography in nuclear medicine consists of two types: single photon emission computed tomography (SPECT) and positron emission tomography (PET). Emission tomography is a functional imaging technique. It provides images of the distribution in the body of a labeled substance, called injected radiotracer, in minute non-toxic amounts. A radiopharmaceutical is most often a biological molecule labeled with half-life radioactive isotopes, which makes it possible to study the functioning of certain organs of the human body. Depending on the tracer molecule, a function of the organism will be explored. In the case of SPECT, the gamma rays emitted by the radiotracer are detected by a gamma camera which, during the acquisition process, revolves around the patient. Rays detected at different angles form two-dimensional projections of the three-dimensional distribution of the radiotracer. In the case of PET, the gamma photons resulting from the annihilation of the positrons emitted by the radiotracer are detected by crystals arranged in a ring around the patient. Two gamma photons detected almost simultaneously form a "coincidence", and the set of detected coincidences form two-dimensional projections of the radiotracer distribution. With the tomographic reconstruction of the projections, it is possible to estimate the three-dimensional concentration of the radiotracer by means of reconstructed sections through the volume. The accuracy of the information extracted from the reconstructed sections is affected by several physical, physiological and technological effects.

1.4 Radiation

The radiation is defined as a transit and the energy comprises electromagnetic radiation, such as X-rays or gamma rays, and particulate radiation, such as neutrons, alpha particles and highly charged ions. Radiation affects people by depositing energy into the body's tissues. The degree of damage depends on the total amount of energy absorbed, the period of exposure, the dose rate and the organs or presentations [3].

1.4.1 Non-Ionizing radiation

According to Yarmonenko[3], radiation can be ionizing or non-ionizing according to the energy emitted. Non-Ionizing radiation cannot ionize matter because its energy per quantum is below the ionization potential of atoms. Near ultraviolet radiation, visible light, infrared photons, microwaves and radio waves are examples of non-ionizing radiation.

Non-Ionizing radiation has enough energy to excite the atoms and molecules, which makes them more vibrant, as evident in a microwave oven, where the radiation vibrates water molecules more rapidly, producing heat.

1.4.2 Ionizing radiation

Ionizing radiation can ionize matter either directly or indirectly because its quantum energy exceeds the ionization potential of atoms. The ionizing radiation concerned are alpha and beta particles, gamma rays and x-rays. The ionizing radiation has enough energy to cause chemical changes by breaking the chemical bonds. This effect can cause damage to living tissue. Different types of ionizing radiation cause similar damage, but all cells in the living body do not react the same way. It was formulated as a law that "the radio-sensitivity of the cells is directly proportional to their reproductive activity and inversely proportional to their degree of differentiation" [4]. Ionizing radiation is defined as a specific type of radiation which causes the elimination of atomic electrons in the tissues they penetrate. This process is called ionization, wherefrom comes the term "ionizing radiation". When such energy is received in appropriate quantities and on a sufficient period of time, it can cause tissue damage [5].

1.5 Medical Uses of Radiation

1.5.1 Radiotherapy

High doses of radiation are used to kill cancer cells when treating tumors in:

- teletherapy, that consists of irradiating tumors with high-energy radiation beams, specifically targeting the tumor to minimize damage to surrounding tissue.
- brachytherapy, that provides a highly localized dose of these methods: either insertion of sealed radioactive sources in the form of rods or threads through hollow tubes in or near the tumor the swallowing of a radioactive liquid that is absorbed selectively by the tumor [6].

1.5.2 Medical Imaging

Radiation imaging is commonly used in diagnostic, such as:

- X-rays to detect injuries or foreign objects in patients;
- Computerized CT scans to create a 3D computer generated image of cross sections of the body;
- Nuclear medicine procedures, when a patient is injected with a radioactive material. This is used in conjunction with a radiation detection instrument to locate tumors and assess organ health [7, 8].

1.6 Radioisotopes in Medicine

The radionuclide is an atom that has an excess of nuclear energy. This energy is released in three different ways:

- a - Energy is emitted by the nucleus in the form of gamma radiation;
 - b - Energy is transferred to one of the electrons of the atom to release the conversion electron;
 - c - The energy is used to create either alpha or beta particles from the nucleus and to emit it;
- During these processes, the radionuclide is said to undergo radioactive decay [9].

1.6.1 Radioisotopes production for nuclear medicine

Cyclotrons and reactors are the two sources of radioisotope production. Cyclotrons can be installed in large hospitals, permitting immediate use. High cost production is achieved by shelling a target with charged particles, usually protons [10]. Nuclear reactors produce radioisotopes in larger quantities at lower cost. The neutron trigger fission in a target containing uranium 235. Radioisotope products should have a sufficiently long half-life to allow their transport. Nuclear reactors provide the production of many gamma emitters and all radionuclides used in therapy and diagnosis. The production of technetium-99m is provided by a "technetium generator" and is delivered to the department of nuclear medicine. The technetium-99m solution is obtained by elution of a chromatographic column of alumina which is a fixed molybdenum 99 (period : 66 hours) [11].

1.6.2 Radiopharmaceutical

Radiopharmaceutical is a radioactive compound used for the diagnosis and therapeutic treatment of human diseases. In nuclear medicine nearly 95% of the radiopharmaceuticals are used for diagnostic purposes, while the rest are used for therapeutic treatment [12]. Radiopharmaceuticals usually have minimal pharmacologic effect, because in most cases they are used in tracer quantities. Therapeutic radiopharmaceuticals can cause tissue damage by radiation. Therapeutic radiopharmaceuticals should be sterile and pyrogen free and should undergo all quality control measurements required for a conventional drug, because they are administered to humans. A radiopharmaceutical may be a radioactive element such as Xe-133 [12], or a labeled compound such as I-131-iodinated proteins and 99mTc-labeled compounds [12]. Radiopharmaceutical has two components: a radionuclide and a pharmaceutical. The usefulness of a radiopharmaceutical is dictated by the characteristics of these two components. In designing a radiopharmaceutical, a pharmaceutical is first chosen on the basis of its preferential localization in a given organ or its participation in the physiologic function of the organ. Then a suitable radionuclide is tagged onto the chosen pharmaceutical such that after administration of the radiopharmaceutical, radiations emitted from it are detected by a radiation detector. Thus, the morphologic structure or the organ's physiologic function can be assessed. The pharmaceutical of choice should be safe and nontoxic for human administration. Radiations from the radionuclide of choice should be easily detected by nuclear instruments, and the radiation dose to the patient should be minimal [12].

1.6.3 Radiopharmaceutical Characteristics

Since radiopharmaceuticals are administered to humans and because there are several limitations on the detection of radiations by currently available instruments, radiopharmaceuticals should possess some important characteristics. The ideal characteristics for radiopharmaceuticals [13] are:

1. Abundant mono energetic gamma ray. Ideally, one would like to have radionuclides with only one photo peak in high abundance in the decay scheme;
2. Energy range from 100 to 300 KeV. This energy range is found to be the most favorable for the gamma camera;
3. No particulate emission. Charged particles such as alpha and beta particles are not useful for nuclear imaging but contribute significant radiation exposure;
4. Short physical half-life. To decrease the radiation dose to the patient, radionuclides with relatively short half lives are desirable;
5. Easy availability for clinical use. For example, the radionuclide is preferably generator-produced and relatively inexpensive;

1.6.4 Physical properties of Yttrium-90

Yttrium-90 is a less pure radioactive beta element (i.e. its disintegration takes place in 100% of cases by beta emission). It is exclusively reserved for therapy or research. [14, 15, 16] Strontium-90 decays into yttrium-90, then zirconium-90; in both cases, it is β -decays, as can be seen in [Figure 1.1]. The half-life of strontium-90 is about 29 years and that of yttrium-90 is 64.10 hours. Zirconium-90 is stable [16].

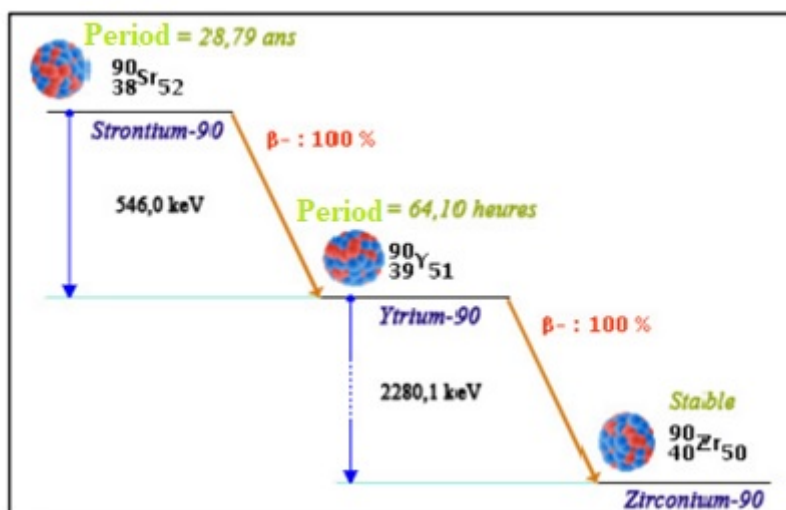


Figure 1.1: Decay pattern of strontium-90 to yttrium-90, to zirconium-90 [16]

The energy emitted during the decay of Yttrium-90 is 2.281 MeV and the average energy is 0.94 MeV. The average path in tissues and water is 11 millimeters, compared to 9 meters in air [16]. The β particles have a discontinuous trajectory in matter. Their energy is important and their trajectory is relatively long. This ability to interact with the material gives them interesting

properties for therapy because their broken path over a long path limits their penetration into the tissues with a large amount of transferred energy. On the contrary, gamma rays, for example, penetrate very well into the material, but requires the use of larger radiation protection means and thicker screens. Therefore, the iodine capsules ^{131}I are placed in sealed chambers, since the iodine ^{131}I is a mixed emitter β and γ . On the other hand, at equal flow rate, the dose rate absorbed at 10 centimeters for a β radiation is greater than that generated by the γ radiation. Exposure of the extremities should be monitored when handling β -radionuclides. Yttrium-90 is one of the main radionuclides used in nuclear medicine therapy. Its high energy, short period and β less pure emission make it a radioelement of reference. It is used in the context of the medical management of certain articular lesions in the form of colloids. In the treatment of lymphomas, Yttrium-90 is associated with an anti-CD20 antibody, ibritumomab tiuxetan, under the patented name Zevalin®. The antibody specifically targets the CD20 antigen of lymphoma cells and yttrium-90 radiates them within a radius of 5 millimeters. The injection takes place over 8 days but does not require hospitalization in a protected room.

1.6.5 Technetium-99m

Technetium 99m is symbolized by Tc-99m, used in tens of millions of medical diagnostic procedures each year [17], making it the most commonly used medical radioisotope. Technetium 99m is used as a radioactive tracer and can be detected in the body by medical equipment (gamma cameras). It is well suited to the role because it emits easily detectable gamma rays with a photonic energy of 140 keV and its half-life for a gamma emission is 6,0058 hours (which means that 93.7% of this cadence decays at Tc-99 in 24 hours). The relatively "short" physical half-life of the isotope and its one-day biological half-life (in terms of human activity and metabolism) enable scanning procedures that allow data to be collected rapidly while limiting total exposure of the patient to radiation. The same characteristics make the isotope only suitable for diagnostic use but never therapeutic. Technetium-99m has been discovered as a cycloélectronique bombardment of molybdenum. This procedure produced molybdenum-99, a radionuclide having a longer half-life (2.75 days), which disintegrated in Tc-99m. Currently, molybdenum-99 (Mo-99) is used commercially as a readily transportable source of Tc-99m for medical use. In turn, this Mo-99 is typically created commercially by highly enriched uranium fission in aging research and material testing in nuclear reactors in several countries [17].

Technetium-99m generators

6-hour half-life of technetium-99m makes storage impossible and would make transportation very expensive. Rather, it is the Mo-99 parent nuclide that is supplied to hospitals after its extraction from neutron targets irradiated with neutrons and its purification in specialized treatment facilities. It is delivered by specialized radiopharmaceutical companies in the form of technetium-99m generators worldwide or directly distributed on the local market. Generators, commonly known as moly cows, are devices designed to provide protection against radiation during transportation and to minimize extraction work in medical facilities. A typical dose rate at 1 meter from the Tc-99m generator is 20 to 50 $\mu\text{Sv} / \text{h}$ during transport. The production of these generators decreases over time and must be replaced every week, (the half-life of ^{99}Mo is still only 66 hours). Molybdenum-99 disintegrates spontaneously at excited states of Tc-99 by beta decay. More than 87% of the decays lead to the 142 keV excited state of Tc-99m. Elec-

trons are easily protected for transport and Tc-99m generators are only minor radiation hazards, mainly due to secondary x-rays produced by electrons (also known as Bremsstrahlung). At the hospital, the Tc-99m that forms through the decay of Mo-99 is chemically extracted from the technetium-99m generator. Most Mo-99 / Tc-99m commercial generators use column chromatography, in which Mo-99 as a water-soluble molybdate, MoO_4^{2-} , is adsorbed on acidic alumina (Al_2O_3). When Mo-99 decays, it forms the TcO_4^- pertechnetate, which, because of its unique charge, is less closely related to alumina. Pulling normal saline through the Mo-99 O_4^{2-} eluted column elutes Tc99m O_4^- soluble, resulting in a saline solution containing Tc-99m in the form of the dissolved sodium salt of pertechnetate [18, 19]. The technetium leaves the generator in the form of the pertechnetate ion, TcO_4^- . The oxidation state of Tc in this compound is +7. This is directly suitable for medical applications only in bone scintigraphy ((as it is absorbed by osteoblasts) and in some thyroid scans (taken instead of iodine by normal thyroid tissue). In other types of Tc-99m-based assays, a reducing agent is added to the pertechnetate solution to reduce the oxidation state of the Tc to +3 or +4. Second, a ligand is added to form a coordination complex. The ligand is chosen to have an affinity for the specific organ to be targeted. For example, the Tc-examinedetrazine complex in the +3 oxidation state is able to cross the blood-brain barrier and cross the cerebral vessels for cerebral blood flow imaging. Sestamibi for myocardial perfusion imaging and mercaptoacetyl triglycine for MAG3 scanning for renal function [20] are other ligands.

1.7 Gamma Camera

At the beginning of the twentieth century, Geiger-Muller was used as a first detection device in nuclear medicine. In 1950, scanning scintigraphs replaced the Geiger-Müller counters [21]. In 1957, the American physicist Hal Anger developed the scintillation camera (gamma-camera) and produced the first prototype that replaced the scanning scintigraphy [22]. The principle of the Anger camera has not changed in 30 years. It has continued to evolve and improve thanks to advances in technology and computing over the last decades. The functions of the gamma camera is to detect and count the gamma photons emitted by the radiotracer in the body, to collect and store information relating to these photons (i.e. position, energy and emission), to determine the location of the points of the gamma camera and provide a representation. A gamma camera is composed of one or more detection heads, each consisting of a collimator, a scintillating crystal where the photons are detected and stopped, a light guide and photomultiplier tubes. An analog or digital circuit is associated with a gamma camera to locate the photons that have been stopped by the crystal. This circuit allows the realization of spectrometry, acquisition and storage of data, their manipulation and online corrections, various procedures related to image processing (display and manipulation).

1.7.1 The detection head

The detection head comprises a collimator, a large surface scintillating crystal, a series of photomultiplier tubes (PM) and a light guide ensuring the coupling between the crystal, the PM and the electronics associated with the image processing. The lead shield is used for the protection of the detector head, the minimization of the detection of radioactive radiation outside the field of vision and the reduction of background noise.

Figure (1.2) shows the components of the detector head.

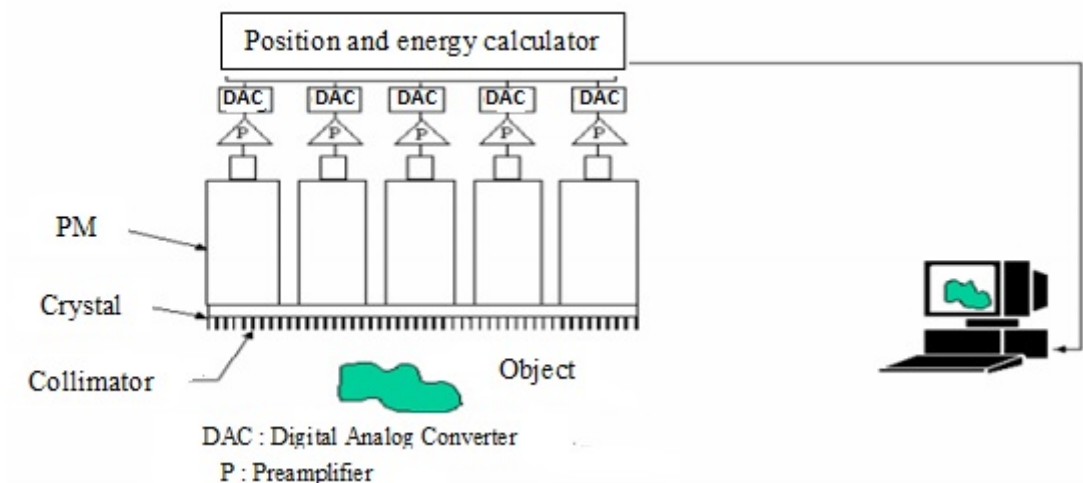


Figure 1.2: The different components of the detection head[24]

1.7.2 Collimator

A collimator is a thick plate (consisting of lead, tungsten, etc.) that is highly absorbent of photons and has cylindrical or conical holes of circular or hexagonal cross-section (see Figure 1.3), according to a specific axis system [23]. Gamma photons, whose path does not follow these directions, are absorbed by the collimator before reaching the crystal. The scintigraphic image is obtained after the collimator corresponds to the projection of the distribution of the radioactivity on the crystal of the detector.

The septum separates the two adjacent holes from the collimator. The lead thickness is calcu-

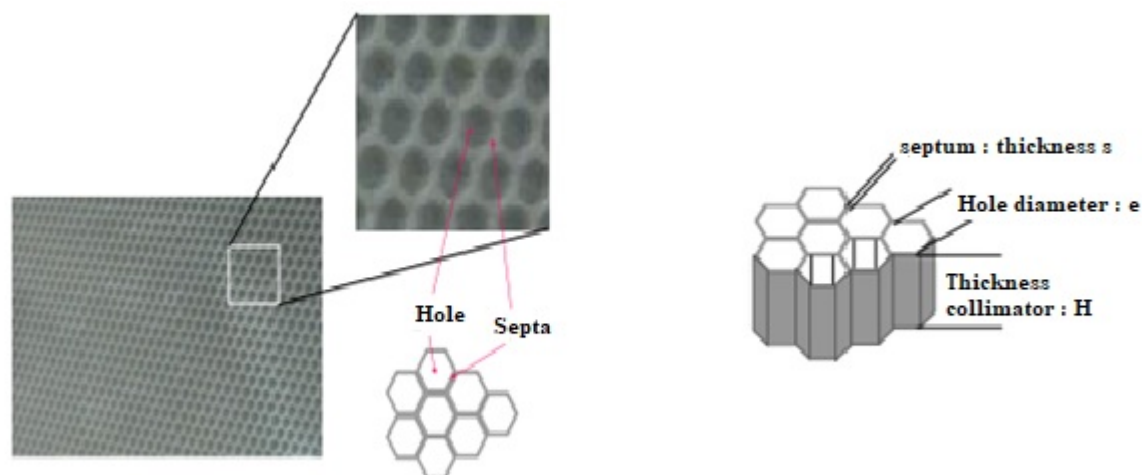


Figure 1.3: A descriptive diagram of a hexagonal collimator [24]

lated to at least 95% attenuation of the photons crossing the septum. The most commonly used collimator is parallel holes. This keeps the dimensions of the image. Also, pinhole collimators

are used for thyroid scintigraphy and fan collimators are used for brain scintigraphy (see Figure 1.4). For collimators with non-parallel holes, the transformation of the dimensions of the image depends on the distance separating it from the collimator [24]. This causes a geometric distortion to consider. The geometric characteristics of the collimator define the field of view, its spatial resolution and the sensitivity of the detection system.

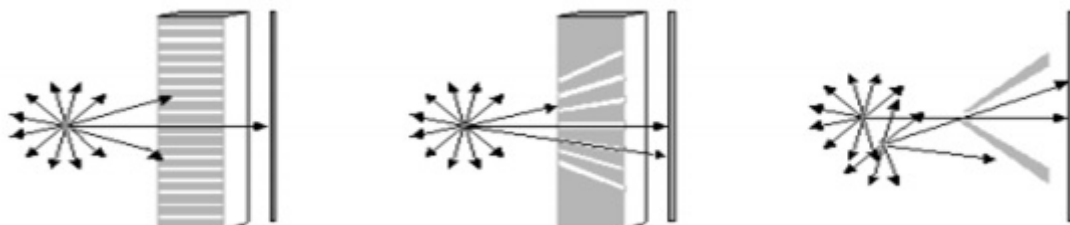


Figure 1.4: The different types of collimator[24]

1.7.3 The scintillating crystal

the scintillating crystal detects the photons emitted by the patient which will be converted into luminous scintillations. The sodium iodide doped with thallium [NaI(Tl)] is often used because it has a density of 3.7 g / cm^3 and a fairly high atomic number ($Z = 53$ for iodine), which makes it possible to stop the majority of photons with energy between 70 and 200 keV over a few millimeters (the range of energy used in clinical routine for single photon emission tomography) [25]. Gamma photons interact with the crystal [NaI(Tl)] by photoelectric effect or Compton effect, producing all or part of their energy. The crystal then emits light photons (scintillations) having a wavelength of about 415 nm (blue-green light in the visible spectrum) well suited to the PM treatment. The scintillator [NaI(Tl)] has also a good luminous efficiency: 13% of the energy deposited is reemitted in the form of fluorescence photons of energy 3 eV (430 nm). It is transparent to its own scintillation light, which prevents scintillation losses by self-absorption. Its time constant of 230 ns makes it possible to record several tens of thousands of hits per second, which allows a high counting rate. Its main disadvantage is its hygroscopic nature (sensitive to humidity) which makes hermetic insulation necessary. In order to protect the crystal from light and moisture and to minimize the loss of scintillation photons, the crystal is often wrapped with a reflector layer (Al_2O_3 , MgO, epoxy, ...) [26]. Finally, since the spectral response of NaI(Tl) is very close to the light response of a bi-alkaline photocathode photomultiplier, the scintillation photons are efficiently collected by the photocathode. The choice of crystal thickness is a compromise between detection efficiency and the spatial resolution, (the thicker the crystal is, the more efficient the detection is, the more the spatial resolution degrades). The properties of NaI(Tl) and other inorganic scintillators commonly used in nuclear medicine (PET and SPECT) are recalled in (Table 1-1).

1.7.4 The light guide

The light guide provides optical coupling between the crystal and the photomultiplier tubes. It is made of a material with a refractive index close to that of NaI (Tl) (1.85), in order to

Scintillator	NaI(Tl)	CsI(Tl)	BGO	CsI(Na)	YAP:Ce	LSO	BaF ₂	GSO
Density(g/cm ³)	3.67	4.51	7.13	4.51	5.37	7.40	1.82	6.71
refractive index	1.85	1.78	2.15	1.84	1.93	1.82	1.5	1.85
λ _{max} (nm)	415	565	480	420	370	420	325/220	440
light response ph/MeV	41000	56000	9000	42000	18000	10000	23000	8200
light response %	100	50	10	85	40	20	75	30
decay time (ns)	230	900	300	630	27	40	630	60
140keV	2.45	3.61	11.63	3.61	1.43	9.34		5.37
511keV	0.328	0.411	0.901	0.411	0.466	0.813		0.674
Hygroscopic	yes	a little	no	a little	no	no	a little	no

Table 1.1: properties of the main scintillators used in nuclear medicine)

optimize the transport of light to the photomultiplier tubes. The shape of the light guide is carefully adapted to the shape of the photocathode of the photomultiplier tube. The light guide also helps to reduce variations in light collection efficiency by photomultiplier tubes. The loss of light caused by the dead space that does not cover the input side of the photomultiplier tubes is reduced by the light guide. This latter collects the light emitted in these dead spaces and directs it towards the photocathode of the photomultiplier tube. In the early gamma cameras, the light guide greatly contributed to improving the linearity of the detection response, but to the detriment of the intrinsic spatial resolution. Currently, the available photomultiplier tubes allow an optimal arrangement on the surface of the crystal (thus a reduction of the dead spaces), and the light guide is replaced more and more by methods of automatic correction of uniformity.

1.7.5 The analog circuit

During scintillation, the emitted light is collected by PM tubes, with the amount of light captured by each PM being inversely proportional to the square of its distance to the point of interaction. In Anger's logic camera (see Figure 1.5), the location of the interaction point of the photon in the crystal and the value of the energy it deposits are determined from the output pulses of all PM by an analog circuit consisting of resistors. Each PM is connected to four resistors, two of which provide the positioning along the abscissa axis (X^+ and X^-) and two others the positioning along the ordinate axis (Y^+ and Y^-). Figure 1.6 shows the device for three PMs along the X axis.

PM tubes of the center deliver substantially adjacent signals for all coordinates while PM corresponding to the most negative coordinates contribute little to the positive coordinates (i.e. the potential measured in X^+). The X and Y coordinates of the interaction are given by:

$$X = X^+ + X^-; Y = Y^+ + Y^- \quad (1.1)$$

We normalize the raw values of the coordinates $X = X^+ + X^-$ and $Y = Y^+ + Y^-$ with respect to the total energy of the treated event, so that the coordinates of the interaction X and

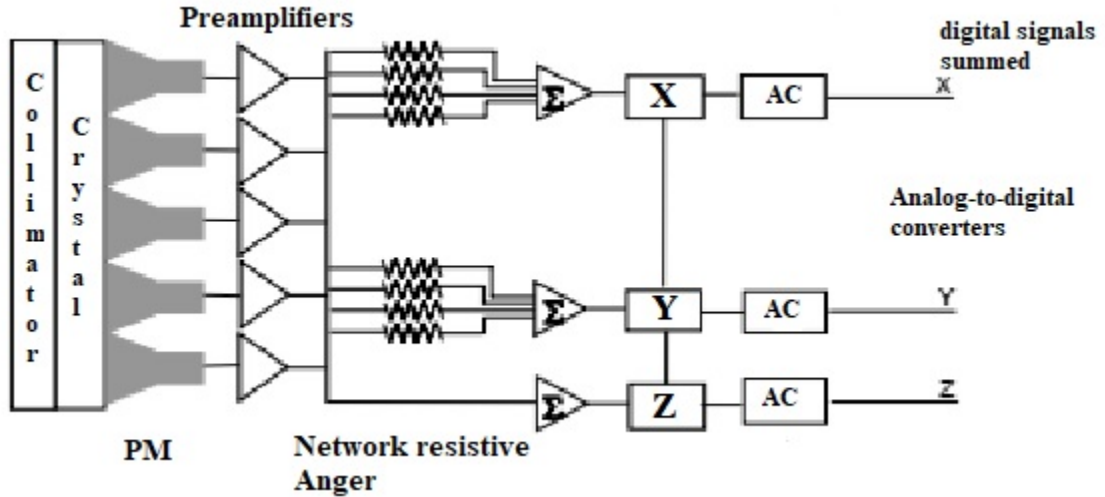


Figure 1.5: Diagram of a gamma-camera of Anger [24]

Y are independent of the emission energy of the radioisotope used:

$$X = \frac{X^+ - X^-}{X^+ + X^-}; Y = \frac{Y^+ - Y^-}{Y^+ + Y^-} \quad (1.2)$$

The amount of energy deposited by the photon during its interaction in the crystal is proportional to the amount of light emitted during the interaction, equal to the sum Z of the signals of all PM:

$$Z = X^+ + X^- + Y^+ + Y^- \quad (1.3)$$

The signal Z is then sent to a single-channel signal analyzer with two discrimination levels, which makes it possible to set a spectrometric window. Current gamma cameras are equipped with two or three analyzers to permit the acquisition of several spectrometric windows simultaneously. Threshold preamplifiers, introduced between the PM and the resistance matrix, have the role of only allowing the pulses of the PM whose amplitude is greater than a predefined value to pass, which has the effect of significantly reducing the fluctuation statistics and result in a gain in spatial resolution. The resistor network is followed by analog-to-digital converters (ADCs) so that the camera can be connected to data acquisition and processing systems. The logic cameras of Anger gradually give way to the so-called "digital" cameras. The major difference lies in the fact that the signal of each PM is digitized individually, and each PM signal is used to calculate the X and Y coordinates independently of Energy.

1.7.6 Processors

The processor on gamma-cameras provide the acquisition and the processing of data, the online corrections of the imperfections and the storage and archiving of data . Not only are processors responsible for the control of the acquisition system, but for the display and manipulation of the images as well.

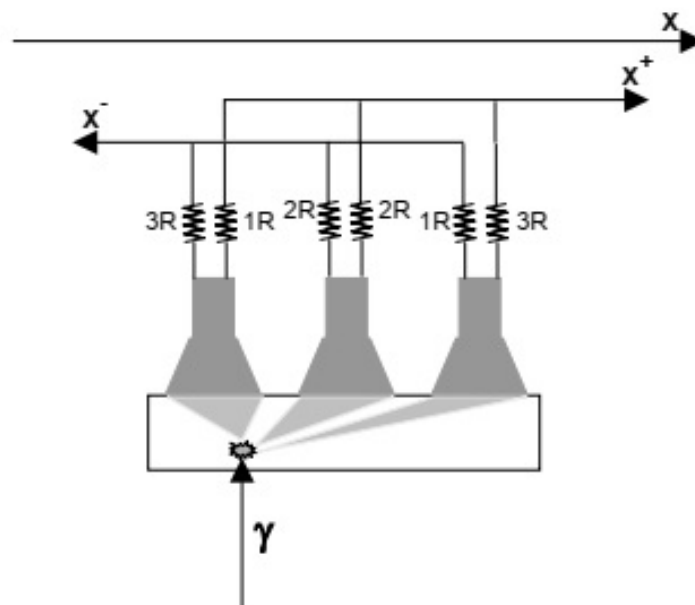


Figure 1.6: Principle of calculating the position of the interaction point in the crystal[24]

1.7.7 Acquisition of data

Acquired data can be stored either in list mode or in frame mode. In list mode, the information relating to a detected photon (spatial and temporal coordinates, energy) is saved in the memory of the processor in the form of a list, which can be read to form any projection by varying the parameters that we want. The incremental mode is more widespread; each acquired projection corresponds to a spectrometric window and is formed as the photons are detected in the spectrometric window concerned. The visualization of the projections in the form of two-dimensional matrices of dimensions 64×64 pixels (or 128×128 pixels, etc.) is simultaneous with the acquisition. For this mode of acquisition, the information (spatial, temporal and energy) of each detected event is no longer accurately known.

1.7.8 Online corrections

The online corrections made by the processor to reduce some of the effects of gamma cameras imperfections, include:

- an automatic adjustment of the PM gain, to verify the calibration of PM and the stability of their performance over time and space;
- an energy correction: the energy response on the surface of the gamma camera is very heterogeneous, which results from several nonuniformity factors in the light collection process, such as the response variability of a PM to the other (quantum efficiency of the photocathode, efficiency of photoelectron collection on the first dynode, gain of the PM) or the variations involved in the collection of light;
- a correction of linearity: the problems of spatial distortions are also related to the structure of the components of the gamma camera (size and number of PM, light guide, crystal, optical counting, etc.) and vary little over time. The correction coefficients of the coordinates (x , y) are calculated and applied in real time during the acquisition of the clinical image.

- Sensitivity correction: Sensitivity defects result from imperfections of the crystal and the light guide and are compensated in real time by the processor, by means of a matrix, typically 64×64 , assigning a multiplicative factor to each pixel.

1.7.9 Data processing

The processor makes it possible to apply different reconstruction techniques (FBP, OSEM, MLEM, etc.) to the images, to process the images in order to reduce the statistical noise or to improve a characteristic, and to apply processes making it possible to extract parameters. Quantitative images are acquired.

1.7.10 Types of acquisition

Static mode

During a static acquisition, the information detected during the acquisition period is used. In static planar mode, the gamma camera remains in a fixed position for the duration of the acquisition. The projections obtained represent a two-dimensional view of the three-dimensional distribution of the radiopharmaceutical in the organ and provide essentially qualitative information on the functioning of the organ. Indeed, obtaining quantitative parameters characterizing a function of the organ will be possible only if an attenuation correction is applied. The success of the examination depends on several parameters, such as the spectrometric acquisition window, the collimator, the waiting time after the injection of the radiotracer and the acquisition time, which can degrade the quality of the image, are poorly adjusted. The spectrometric window must be chosen according to the emission energy of the radiopharmaceutical used while the collimator must be chosen in order to define a field of view corresponding to the size of the organ studied and to offer a sufficiently high sensitivity to provide a satisfactory image quality. Typically, the waiting time after the injection and the acquisition time depend on the organ studied and the nature of the radiotracer. Static acquisitions can also be performed in tomographic mode.

Dynamic mode

Dynamic acquisitions consist of acquiring a sequence of images spaced in time, which provides useful quantitative information on the functioning of organs, such as the heart, kidneys or lungs. The acquired data are processed to produce "activity-time" curves describing the rates of fixation or elimination of the radiopharmaceutical in the organ. Functional parameters of images (parametric images) extracted from the acquisitions may be formed to condense the information contained in a large amount of data. Acquisitions may be planar or tomographic. The most encountered applications are:

- Dynamic cardiac imaging: The measurement of the left ventricular ejection fraction is obtained from acquisitions synchronized with an electrocardiogram (ECG) and consists in determining the quantity of blood, averaged over many heartbeats, entering the arterial system of the body and coming from the left ventricle. This measurement provides information on the normal or abnormal functioning of the heart and allows the prognosis of infarction or coronary events;

- dynamic kidney imaging: temporal images of the kidneys are used to plot renograms, which represent the radioactive activity in the kidney over time and provide information on the functioning of the kidney. The three major phases of renal function (perfusion, filtration and excretion), visible on the renogram, allow to highlight the success or failure of a transplantation, to check the intrinsic functioning of the kidney and to highlight problems of urethral obstruction or reflux (return of urine from the bladder to the kidney). Other applications in dynamic planar scintigraphy include studies of the brain, lungs, liver, etc.

Multi-isotopic mode

This technique is used when there is no known radiotracer with a high specificity towards a target organ. Two different radiopharmaceuticals are used, having a different tropism for the target tissue: the first is, for example, fixed on both healthy and diseased tissues and the second only on healthy tissues. Two images are made, sometimes simultaneously to reduce motion artifacts, in two separate spectrometric windows corresponding to the photoelectric peak of each of the two radiotracers. The distribution of radioactivity corresponding to the diseased tissue is deduced by subtraction (sometimes by comparison) of the two images. These multi-isotopic studies can be performed in planar or tomographic mode, and in static or dynamic.

Tomographic mode

Monophoton Emission Tomography is a technique in which the gamma camera describes a circular or elliptical orbit around the patient and provides two-dimensional projections under various incidences. The implementation of the SPECT provides, compared to the planar scintigraphy, a contrast enhancement between the regions of different functions, a better spatial location, an improved detection of the abnormal functions, and especially an improvement of the quantification. In the case of so-called "transaxial" tomography, the reconstructed sections are perpendicular to the detection face of the gamma-camera. The gamma camera provides a set of 2D images, or projections, consisting of multiple profiles, each profile representing a 1D projection of the radioactivity in a single section of the patient. Thus, the 3D object is divided into multiple 2D sections and each section is represented by a set of discrete 1D profiles. Each point of the profile represents the linear sum (in the absence of attenuation) of the elements of activity along the line of sight of the detector as determined by the collimator. If many linear and angular data are acquired, it is then possible to reconstruct sectional images that represent the distribution of the radiopharmaceutical in the body. A tomographic acquisition has 128 projections, each of which includes 128×128 pixels and acquired for 64 (or 128) values of discrete angles covering 360° around the patient. By using reconstruction algorithms, it is possible to obtain transaxial section images, sagittal, and coronal.

1.8 Performance of a gamma-camera: Evaluation and Potential improvements

The performances of a gamma-camera are characterized by: spatial resolution, energy resolution, sensitivity, uniformity and linearity. Each of these parameters depends on the characteristics of the different components of the detection head and are very often correlated. These

performance evaluation parameters are first clarified, then we take stock of the various technologies existing or under development to improve some of these performances.

1.8.1 Performance of a gamma-camera: Evaluation

Spatial resolution

The spatial resolution R of a detector describes the degradation that it introduced during the acquisition of the image of a point or a linear source. This degradation results in the observation on the image of a spot. Spatial resolution is the smallest distance between two-point sources as these are recognizable on the acquired image. It is measured by the half-value (FWHM) width of the point spread function (PSF) or linear, obtained by the image of a point source or a linear source, respectively. The spatial resolution R of the gamma camera is the result of the contribution of the intrinsic spatial resolution R_I related to the characteristics of the crystal and the associated electronics and the spatial resolution of the collimator R_C to the source-collimator distance:

$$R = \sqrt{R_C^2 + R_I^2} \quad (1.4)$$

The measurement of the intrinsic spatial resolution R_I is made on the useful field of the camera without collimator. The intrinsic spatial resolution depends on the random distribution of recoil electrons resulting from the interaction of the gamma photons in the crystal, the statistical fluctuations in the number of optical photons reaching the photocathode of the photomultiplier tubes, the quantum efficiency of the photomultiplier tubes and the calculation of the point of impact by the positioning electronics. At 140 keV, it is typically 3 mm for current cameras. The resolution of the collimator depends on the geometry of the collimator: for a parallel collimator (see Figure 1-7), the geometric spatial resolution R_C is expressed approximately according to the dimensions of the collimator [42]:

$$R_C = \frac{\left(\frac{e}{e+s}\right)(H_e + b + d)}{H_e} \quad (1.5)$$

Where e , s , b , d and H_e respectively denote the diameter of the holes of the collimator, the thickness of the septum, the distance between the collimator and the source and the front face of the collimator and the effective length of the channels, calculated taking into account the height of the collimator H and the attenuation coefficient μ of the material constituting the collimator:

$$H_e = H - \frac{2}{\mu} \quad (1.6)$$

As shown in Equation 1.5, the spatial resolution of the collimator increases almost linearly as the source-collimator distance increases. This same equation shows that spatial resolution can be improved by increasing the length of holes and the number of holes per unit area, or by minimizing the distance between the source and the surface of the collimator. The choice of the collimator will therefore be based on the energy of the radioisotope used and on considering an acceptable compromise between spatial resolution and sensitivity.

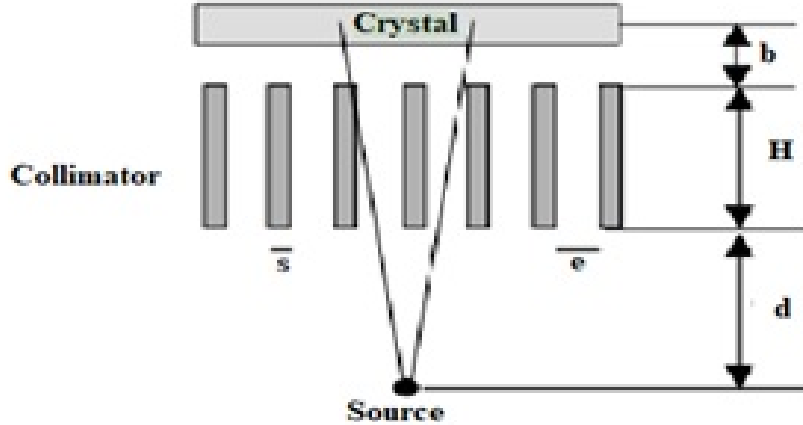


Figure 1.7: Parameters of a parallel collimator

Energy resolution

The energy resolution reflects the determination of the energy of a detected photon. The imperfect measure of energy results from statistical fluctuations in the number of optical photons emitted by scintillation, those of the quantum yield of photocathodes and the gain of photomultiplier tubes and acquisition electronics. As a result, the spectrum of lines corresponding to the photoelectric absorption peaks of the photons in the crystal that should ideally be obtained must be convoluted by the energy response function of the gamma camera. The energy resolution $FWHM(E)$ is measured by the half-height width ΔE of the energy response of the gamma camera for the emission energy E of the radioisotope used and is expressed in %:

$$FWHM(E) = \frac{\Delta E}{E} \times 100 \quad (1.7)$$

The energy resolution for current gamma cameras is on the order of 10% to 140 keV. The energy resolution varies non-linearly with the energy according to the law [43]:

$$FWHM(E) = f\left(\frac{1}{\sqrt{E}}\right) \quad (1.8)$$

The function f must be precisely parameterized to correctly model the energy response of a given gamma camera over a given energy range, each gamma camera having in theory an energy response of its own. The limited energy resolution of a gamma-camera introduces an uncertainty as to the differentiation of the primary photons, i.e. those belonging to the total absorption peak and having interacted by photoelectric effect in the crystal, and the scattered photons, that is, those having Compton diffusion. Photons that scatter at a low angle retain much of their initial energy. For example, a photon that diffuses at a 52° angle will produce a scattered photon of energy equal to 126 keV, which will be detected in the conventional spectrometric window of acquisition centered on the emission energy of the radioisotope and having a width at half height equal to 20% of this emission energy (for Tc-99m, this window is between 126 and 154 keV). Even if in practice the acquisition spectrometric window is chosen to remove many scattered photons, scattered photons are superimposed on the primary photons in this spectrometric window: for example, for acquisitions at Tc-99m, it is estimated that about 30% the proportion of scattered photons are detected in the 20% window [29].

1.8.2 Sensitivity

The sensitivity is defined by the ratio of the number of primary photons detected (photons that have not undergone any interaction before reaching the crystal) to the total number of photons emitted by the radioactive source at the solid angle seen by the detector. The sensitivity depends mainly on the type of collimator used and the light output of the crystal. For a parallel collimator, the geometric sensitivity S_C is defined as the fraction of radiation emitted by a point source that passes through the collimator channels. It is given by [30] :

$$S_C = \left[\frac{e^2}{H_e(e + s)} \right] \quad (1.9)$$

The equation (1.9) shows that the sensitivity for a parallel collimator is independent of the distance between the source and the surface of the collimator.

1.8.3 Spatial linearity

Spatial linearity characterizes the ability of the gamma camera to precisely determine the coordinates of the interaction of the photon in the crystal: it is the ability to restore the exact shape of an object. It can be measured by analyzing the geometric distortions induced in the reproduction of an image of linear sources. Poor linearity introduces image distortion and troublesome field homogeneity in tomographic mode. These linearity defects depend strongly on the homogeneity of the photocathode response of the photomultiplier tubes, the number of tubes used, the homogeneity of the crystal and the light guide when present [30]. Spatial distortions were minimized by increasing the number of photomultiplier tubes equipping the gamma cameras and selecting tubes with more homogeneous photocathodes. The defects that persist are corrected directly on the image acquired by the processor

1.8.4 Uniformity

The uniformity of a gamma camera defines the ability of the gamma camera to produce a homogeneous image when exposed to a homogeneous flow of photons. Uniformity can cause very important artifacts in tomography: small localized variations in uniformity, of the order of 5%, can cause circular artefacts to form on the images [31].

1.8.5 The Image Quality in Nuclear Medicine

In nuclear medicine, the basis of image quality is the ability of the imaging device to detect differences in the uptake of a radiopharmaceutical in a lesion and its surroundings. Hence, an image of high quality is one that can reproduce this contrast in order to secure a correct diagnosis. However, several factors will degrade the image quality, some of which are due to inherent properties of the imaging device such as spatial resolution, energy resolution, non-uniformity, or distortions. Other degrading factors depend on the patient and organ localization. A large patient will increase the influence of scattered photons. An organ deep in the body will be overlapped by other tissues, which will increase the background registrations. Patient and organ movements will also degrade the image quality. There are some important factors due to the operation of the imaging device and they can be optimized by the user. These include spatial

resolution by keeping the distance between the detector and the patient as short as possible and noise reduction by selecting an optimum examination time and matrix size. Scattered radiation can be reduced by a proper setting of the pulse height analyzer.

1.8.6 Contrast

Contrast is a measure of the difference in image intensity between adjacent regions in the image. The contrast in a planar image should ideally reflect a 2D projection of the activity distribution within the patient. In SPECT, the contrast is improved compared with a planar image, since there is no contribution from over- and underlying activities in the calculated 3D activity distribution. In this case the contrast should ideally reflect the activity distribution in the different tissues. The contrast can however be influenced by attenuation, scattering, septal penetration and background radiation. For small objects, spatial resolution will also have a high impact on image contrast. Various equations for calculating the contrast can be found in the literature [13]. The following equation was used to calculate the contrast:

$$\text{Contrast} = \frac{C_s}{C_b} - 1 \quad (1.10)$$

$C_s = N_s/V_s$: Number of counts in the lesion (spheres) per voxel

N_C : Total counts in the lesion

V_s : Lesion volume in number of voxels

$C_b = N_C/V_B$: number of counts in the background compartment per voxel

N_C : Total counts in the background compartment

V_B : Background volume in number of voxels

1.8.7 Factors Affecting Image Contrast [77]

Perhaps the major factor affecting contrast is added background counting rates that are superimposed more or less uniformly over the activity distribution of interest. Background counting rates can arise from a number of sources. Septal penetration and scattered radiation are two examples. Another would be inadequately shielded radiation sources elsewhere in the imaging environment. Septal penetration is avoided by using a collimator that is appropriately designed for the radionuclide of interest. Scattered radiation can be minimized by pulse-height analyzer; however, sodium iodide [NaI(Tl)] systems cannot reject all the scattered radiation and rejection becomes especially difficult for γ -ray energies below approximately 200keV, as illustrated by Figure (1-8). Using a narrower analyzer window for scatter rejection also decreases the recorded counting rate and increases the statistical noise in the image. A reasonable tradeoff between counting efficiency and scatter rejection for imaging systems using NaI(Tl) detectors is obtained with a 15% energy window centered on the γ -ray photo-peak. Primary spectrum refers to γ rays striking the detector without scattering from objects outside the detector. Scatter spectrum refers to γ rays that have been scattered by objects outside the detector, such as from tissues or other materials surrounding the source distribution. (Adapted from Eichling JO, TerPogossian MM, Rhoten ALJ: Analysis of scattered radiation encountered in lower energy diagnostic scanning. In Gottschalk A, Beck RN, editors: Fundamentals of Scanning. Springfield, IL, 1968, Charles C Thomas). There has been continuing interest in applying semiconductor

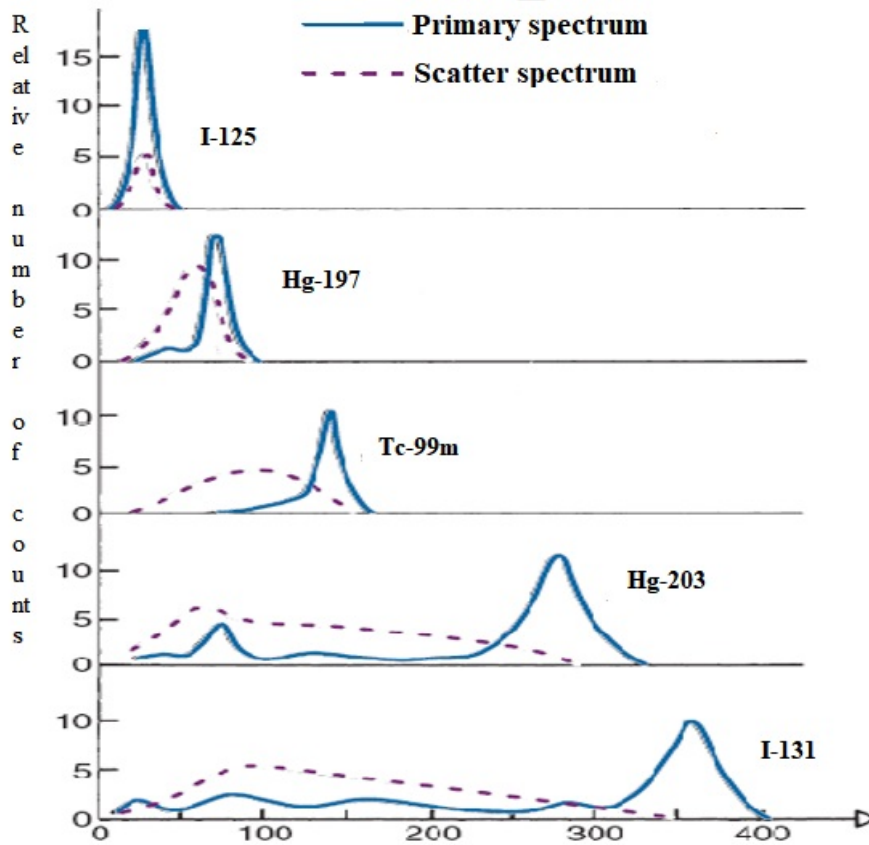


Figure 1.8: Pulse-height spectra recorded with a NaI(Tl) detector for different γ -ray energies

detectors to nuclear medicine imaging to take advantage of their superior energy resolution for discrimination against scattered radiation by pulse-height analysis (Figure(1.9)).

In the NaI(Tl) spectrum, the blue curve represents unscattered (primary) γ rays, the orange curve represents γ rays scattered by materials around the source, and the red curve represents the sum of the primary and scattered γ rays. For the Ge(Li) detector (bottom), only the spectrum for primary γ rays is shown. Separation of primary from scattered γ rays is much easier with the semiconductor detector. An important contributor to background radiation in conventional planar imaging is radioactivity above and below the object of interest. Image contrast is improved in emission computed tomography (SPECT and PET), because it permits imaging of an isolated slice without the superimposed activities in overlying and underlying structures. Tomographic techniques offer significant improvements for the detection of low-contrast lesions. Figure (1.10) illustrates this effect. Note the improved contrast and visibility of the voids in the cardiac portion of the phantom when overlying and underlying activity are removed in the SPECT images. (Courtesy Dr. FreekBeekman, Delft University of Technology, Netherlands.)

1.8.8 Noise

Improved image quality owing primarily to the random (Poisson) nature of radioactive decay, noise is an inherent component of nuclear medicine imaging. If an interaction in the NaI(Tl) crystal in the gamma camera is accepted to contribute to the image, one count will be added to the image pixel corresponding to the location of the photon interaction. Each pixel in the

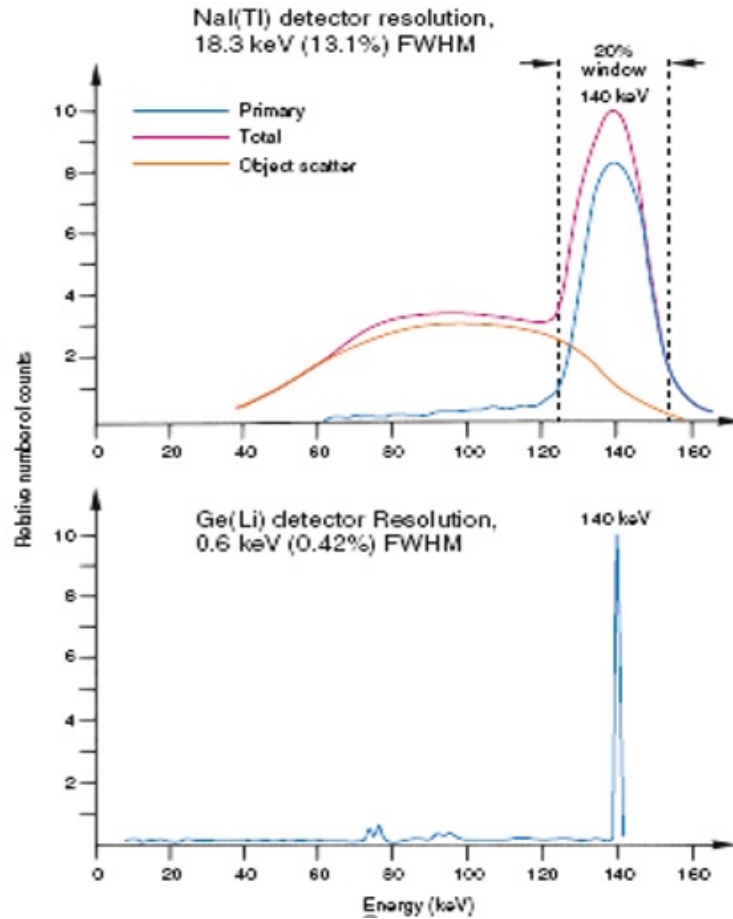


Figure 1.9: Comparative pulse-height spectra recorded from a ^{99m}Tc source with NaI(Tl) and Ge(Li) detectors

raw data image can therefore be viewed as a photon counter, and the probability of detecting x photons is then described by the Poisson distribution:

$$P(x) = \frac{\bar{x}^x e^{-\bar{x}}}{x!} \quad (1.11)$$

Where, x is the expected number of detected photons (the mean value in a homogeneous region or in repeated identical measurements). The standard deviation of the Poisson distribution is calculated from this equation:

$$s = \sqrt{\bar{x}} \quad (1.12)$$

If x is large, at least in the order of 15, the Poisson distribution can be approximated with a Gaussian distribution. Noise is usually calculated as a percentage of the standard deviation divided by the mean value. The limited amount of activity that can be given to the patient, the limited examination time and the construction of the collimator are factors that contribute to a high noise level in comparison with other diagnostic techniques. The noise level is often higher than 10% in SPECT projection images, but is in most cases lower in planar scintigraphic images due to the longer measurement time per image [13].

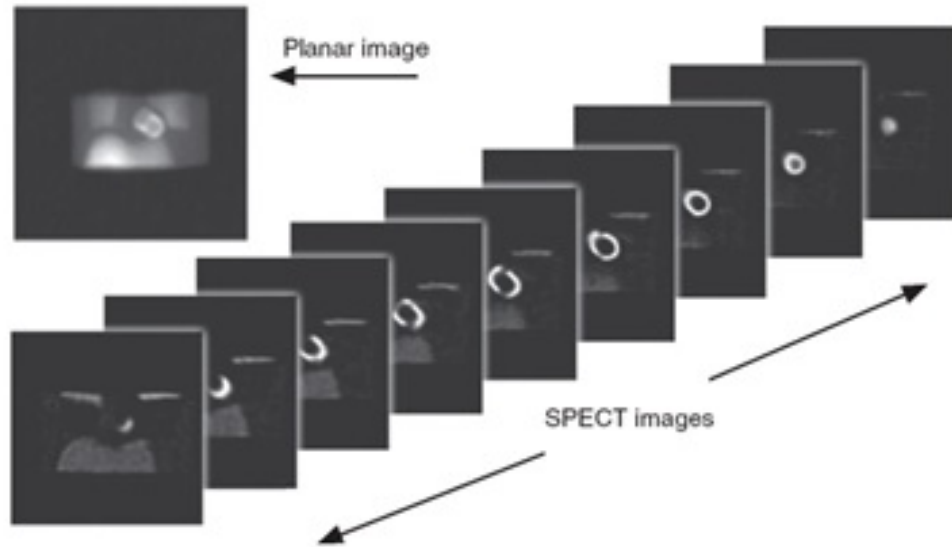


Figure 1.10: Planar (upper left) and single-photon emission computed tomographic (SPECT) (center) images of a thoracic phantom

1.9 Limits of SPECT imaging

Many factors affect the qualitative and quantitative accuracy of images obtained in SPECT [32], among which physiological factors relating to the patient (such as emission and kinetics of the radiotracer and patient movement), technological factors (performance of detection system) and physical factors (attenuation, diffusion and measurement noise) can be found.

1.9.1 Physiological factors

Several physiological factors contribute to reducing the number of photons detected during an acquisition, and in fact limits the quantification of images (these are factors associated to the characteristics of the radiopharmaceuticals and related factors to the patient). Currently available radiotracers are not totally specific and attach to other organs, creating background activity. For example, fixation by the liver is very great for many radiotracers because of the very function of this organ. This limitation results in a loss of contrast and detection statistics. In addition, the dose that can be administered to the patient is limited by a critical irradiation dose not to be exceeded. The acquisition time is also an important parameter: it is often set to acquire enough statistics to obtain good quality images and taking into account the tolerance of the patient during the examination. Finally, the size of the patient affects the fraction of attenuated photons and the fraction of scattered photons, which contributes to reducing the number of photons detected.

1.9.2 Physical factors

Physical factors correspond to photon interactions in the patient's body and the gamma camera. Three factors affect the quantification of absolute radioactivity, depending on the radiotracer

used and the morphology of the patient:

- the attenuation of photons by the tissues crossed,
- the scattering of photons in the patient and the detector,
- the measurement noise resulting from the statistical nature of the photon emission and the noise affecting the detected signal.

1.9.3 Attenuation

Description of the physical phenomenon

When a photon beam passes through the material, the number of photons initially present in the beam decreases: the attenuation of the beam denotes the loss of these photons, either by photoelectric absorption or by diffusion at a sufficiently wide angle so that they do not disappear. The number N of photons transmitted after crossing a medium of thickness x (in cm) is thus given by an exponential attenuation law:

$$N = N_0 \times e^{-\mu x} \quad (1.13)$$

The linear attenuation coefficient μ represents the probability of interaction of one photon per unit of length and is expressed in cm^{-1} . Linear attenuation coefficient and interaction cross section σ are related by the relation:

$$\frac{\mu}{\rho} = \frac{N_A}{A} \sigma \quad (1.14)$$

Where, ρ : represents the density of the traversed medium (g/cm^3),

N_A : the number of Avogadro (in atom mol^{-1}), A : the atomic mass of the medium (in g / mol) and σ the total cross section (in $cm^2/atom$). The interactions responsible for attenuation are photoelectric effect, Compton scattering, Rayleigh scattering, and pairing. At energies typically less than the MeV involved in medical imaging, the creation of pairs is not concerned since it requires a threshold energy of 1.022 MeV (2×511 MeV) to create the two photons of the pair.

Photoelectric effect

A photon is absorbed by an electron linked to the atom called a photoelectron, which is ejected with a kinetic energy $E_{kin} = h\nu - E_b$, where E_b is the binding energy of the electron on its original electronic layer. The photoelectric effect mainly concerns the most connected electrons. Photoelectrons are emitted in all directions of space, but with a preferential direction that depends on the energy $h\nu$ of the incident photon. For low energy photons, the distribution is practically symmetrical with respect to $\theta = 90^\circ$, where θ is the angle between the direction of the incident photon and that of the emitted electron. When $h\nu$ increases, θ tends to zero. In the photoelectric effect there is always a rearrangement of the electron cortege of the atom, with a characteristic emission of X-rays or Auger electrons which carry away the excitation energy. The photoelectric effect is the predominant mode of interaction of gamma or X radiation with energy below 100 keV. It is highly favored in the middle of high atomic number and decreases very rapidly when the energy increases. It is essentially with electrons K (more than 80%) that the photoelectric effect occurs.

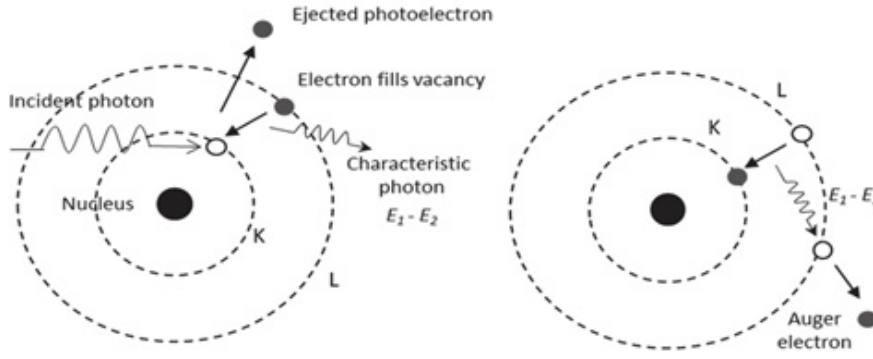


Figure 1.11: Photoelectric effect

Compton scattering

It is the interaction of a photon with a weak electron of the absorbing medium (Figure 1.12). The photon is scattered in a direction θ with respect to the incident direction and yields a

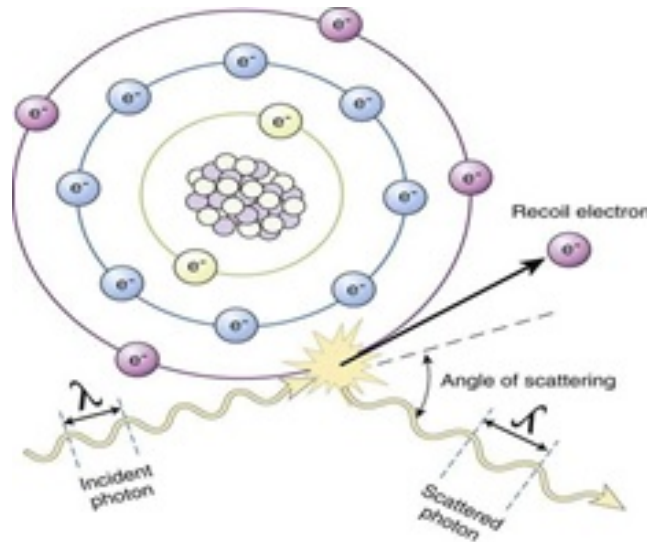


Figure 1.12: Compton scattering

fraction of its energy to the electron, which moves back in a direction ϕ with respect to the incident direction. By writing the laws of conservation in energy and momentum, one obtains the formulas concerning the energy of the diffused photon and the electron of recoil. In the following calculations, the binding energy of the electron is neglected because the Compton effect concerns the loosely bound electrons of the outer electron layers of the atom. The energy of the scattered photon $h\nu'$ is given by:

$$h\nu' = \frac{h\nu}{1 + \alpha(1 - \cos\theta)} \quad (1.15)$$

where $h\nu$ is the energy of the incident photon, m_0c^2 the mass energy of the electron, and

$$\alpha = \frac{h\nu}{m_0c^2} \quad (1.16)$$

The energy of the scattered photon is maximum for $\theta = 0$, where $h\nu' = h\nu$, and minimum for $\theta = 180^\circ$, which corresponds to the phenomenon of backscattering. For low energies $h\nu$, distribution depends little on the angle θ . On the other hand, at high energies, the photons are diffused preferentially towards the front.

1.9.4 Noise measurement

The noise corresponds to a statistical fluctuation superimposed on the signal and possibly coming from the detector (emission and counting noises) or reconstruction. Throughout the detection chain, be it the radioactive emission of photons, the creation of photoelectrons in the crystal, their conversion into electrons by the photocathode, processes of a stochastic nature take place and follow a law of Poisson. The presence of a Poisson noise introduces errors in nature and influences the signal-to-noise ratio.

1.10 Conclusion

We have recalled in this chapter the principles on which Monophotonic Emission Tomography is based as well as the limits imposed on this modality by many factors. Particular attention has been paid to the technological limitations that affect the performance of the detection device: a review of the improvements studied recently or under development concludes that technological solutions can improve these performances only at the cost of implementing complex and expensive technologies. The performance of the gamma camera type Anger has been improved over the years, but the principle of the camera itself is still the same. Solutions have been developed or are being developed to improve intrinsic spatial resolution and energy resolution as well as sensitivity, but involve increasingly complex and expensive technologies. Despite these efforts, the collimator remains the most penalizing and unavoidable device. Up to date, there is no solution that has provided a sensitivity exceeding that obtained with other imaging modalities, such as PET, scanner or MRI. This aspect limits the quality of the diagnosis that can be obtained from SPECT images in addition to the intrinsic limits associated with the detection system. The presence of the collimator is also a serious penalty in terms of spatial resolution and sensitivity. Other technological limits are due to the physical phenomena of attenuation, diffusion, variation of the spatial resolution of the camera and measurement noise. The physical origin and description of these phenomena are provided in this chapter and their effects on the quality and quantification of images are underlined. It is essentially a degradation of the spatial resolution and a contrast of the reconstructed sections that lead to errors in the quantification of images to artifacts, and affect the estimation of reliable dimensions and concentrations.

Chapter 2

State of the Art of Monte Carlo Simulation Codes Used in Nuclear Medicine

2.1 Introduction

Numerical simulations are used in different scientific fields because they make it possible to reproduce by calculation a physical phenomenon whose behavior described by a system of mathematical equations must be evaluated. They produce data very close to reality and thus provide approximate solutions to complicated problems that are even expensive to solve with an experimental approach. Their exploitation in the field of medical imaging has greatly increased in recent years to study and develop new virtual imaging devices. There are two main types of numerical simulations: deterministic methods that solve the problem analytically from a set of model equations and probabilistic methods using Monte Carlo simulations. Analytical methods consist of modeling a physical phenomenon from a system of equations with as many relationships as unknown parameters. Thus, particle tracking is modeled from the equations that describe their transport in matter. The disadvantage of these methods is that only the primary beam is modeled, the scattered photons cannot be considered. They therefore lead to theoretical results which, in some cases, do not correspond to reality and therefore lack precision. Nevertheless, they remain feasible and effective for small calculations. Monte Carlo simulations are interesting for modeling configurations that are too complicated for an analytical simulation. These are stochastic methods based on the drawing of random numbers as a function of probability density functions representative of the processes studied. They make it possible to simulate stochastic phenomena such as the emission, transmission or transport of particles in matter to give their probability of interaction with the medium. They are particularly well suited to medical imaging.

2.2 Monte Carlo simulations

2.2.1 Principle of the Monte Carlo method

The principle of a Monte Carlo simulation is to generate a series of random numbers with a uniform distribution between 0 and 1 with a probability density function $f(x)$ defined by:

$$f(x) = \begin{cases} 1 & \text{for } 0 \leq x \leq 1 \\ 0 & \text{else} \end{cases} \quad (2.1)$$

The sequence $\{x_1, x_2, x_3 \dots x_n\}$ is then used to generate another sequence $\{y_1, y_2, y_3 \dots y_n\}$ of random numbers distributed as a function of the function g of the desired probability density (y) . In practice, the sequence of random numbers whose probability of appearance in each print is identical, we obtain from the so-called pseudo-random generator numbers, the latter is present in the libraries of programming languages C and C++. The term "pseudo" comes from the fact that it is impossible to generate real random numbers using computer code. Thus, generators produce sequences of numbers whose properties are as close as possible to random numbers. They are most often based on a linear congruence algorithm easy to program and initially introduced in 1948 by Lehmer [32]:

$$X_{n+1} = (ax_n + b) \bmod(m) \quad (2.2)$$

This type of generator produces a sequence of pseudo-random numbers between 0 and $m-1$, which is therefore m period. By dividing the results obtained by m , we obtain a sequence of numbers distributed uniformly over $[0,1]$. The probability distribution obtained between 0 and 1 is therefore uniform. The effectiveness of a Monte Carlo code depends largely on the statistical quality of the random draws and therefore the random number generator used. The Mersenne Twister generator, proposed by Matsumoto and Nishimura (1997), is renowned for its quality and speed of execution compared to most other generators; it is therefore very used in numerical simulations. The pseudo-random numbers thus generated are then used to sample the probability density functions of the different processes to be simulated. There are different sampling methods, including the inversion method and the rejection method. Let x be the random variable to be sampled and $f(x)$ be the corresponding probability density function, defined over an interval $[x_{min}, x_{max}]$. The cumulative distribution function $F(x)$ (or the cumulative probability density of $f(x)$), with values in $[0,1]$ and defined so that $F(x_{min}) = 0$ and $F(x_{max}) = 1$, wrote:

$$F(x) = \int_{x_{min}}^x f(u) du \quad (2.3)$$

The random variable x can be sampled using pseudo-random numbers, uniformly distributed between 0 and 1, according to one of the following two methods.

2.2.2 Inversion method

This method is used when the cumulative distribution function $F(x)$ of the random variable x can be reversed. If we consider that $F(x)$ varies uniformly between 0 and 1 in the interval $[x_{min}, x_{max}]$, to a random number R defined in the interval $[0,1]$, we can associate x such that:

$$R = F(x) = \int_{x_{min}}^x f(u) du \quad (2.4)$$

The sampled value x is obtained by inverting the cumulative distribution function according to the following equation:

$$x = F^{-1}(R) \quad (2.5)$$

The inversion sampling method is the most straightforward and simplest simulation method to implement. It can be used whenever the cumulative distribution function $F(x)$ is invertible and the probability density function $f(x)$ is positive and integrable.

2.2.3 Rejection method

The rejection method is an alternative method to the inversion method and will be used when the cumulative distribution function $F(x)$ of the random variable x cannot be reversed. It can be broken down into several steps:

1) definition of a normalized function $f'(x)$:

$$f'(x) = \frac{f(x)}{f_{max}(x)} \quad (2.6)$$

where $f_{max}(x)$ represents the maximum value of $f(x)$

2) drawing a random number R uniformly in the interval $[0,1]$ and then determining its corresponding value in the variation range $[x_{min}, x_{max}]$ according to the following relation:

$$x = x_{min} + (x_{max} - x_{min}) \times R \quad (2.7)$$

3) Drawing a second random number R' , uniformly distributed between 0 and 1;

4) Comparison of R' with respect to the normalized function $f'(x)$:

If $R' < f'(x)$: the sampled value x is accepted; Otherwise the numbers R, R' are rejected and two new random numbers are drawn.

The series of values of x that have been accepted are distributed according to the function $f(x)$. Unlike the inversion method, the rejection method requires two draws per iteration instead of one. In addition, it can be inefficient if the number of prints is important. The rejection sampling method is, for example, used to determine the scattering angle and the corresponding energy of the scattered photon after Compton interaction.

2.2.4 Application of Monte Carlo methods

In the field of particle physics, Monte Carlo simulations consist in carrying out, for each stochastic process, a random draw according to the corresponding probability density function (exponential decay law, differential absorption or diffusion cross section, depositions of energy, effect of resolution of the detector ...). Several random number draws are sometimes required for each step of the physical process. The Monte Carlo simulations used in this thesis work were made from radioactive sources emitting mainly γ photons. We therefore chose to present the different stages of the Monte Carlo simulation of a γ photon in the material (Figure 2.1). At first, the decay of the radioactive source is simulated according to an exponential decay law allowing to know the number of particles emitted at a given instant t given $N(t)$, as a function of the initial number N_0 of radioactive nuclei:

$$N = N_0 \times e^{-\frac{\ln(2)}{\tau}t} \quad (2.8)$$

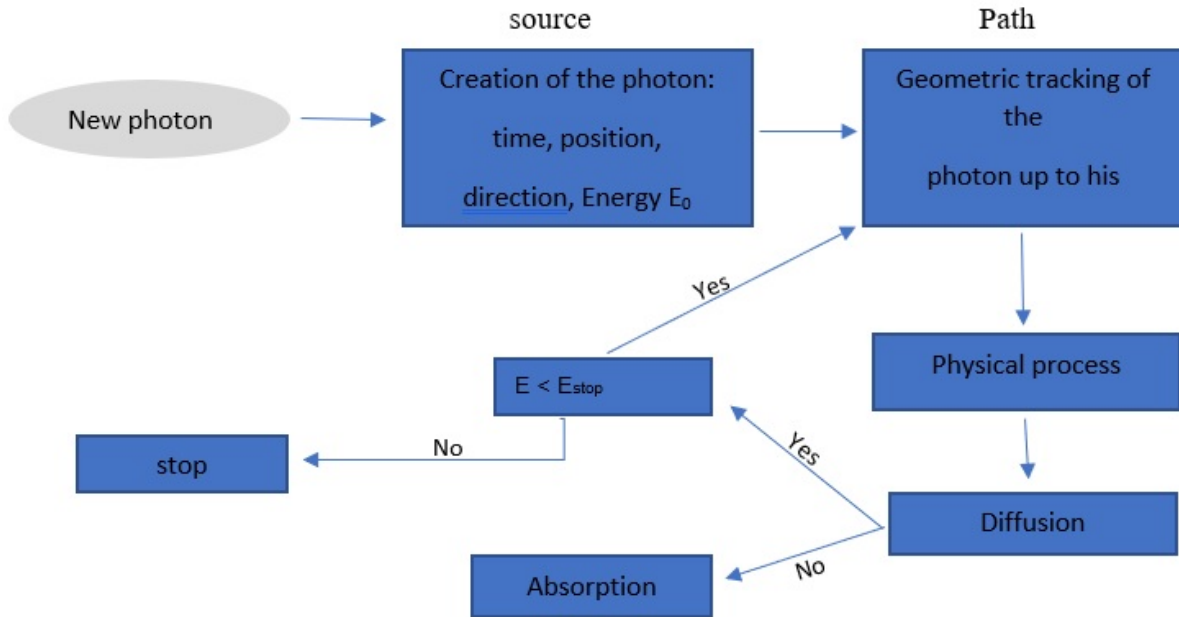


Figure 2.1: The different stages of the Monte Carlo simulation

where τ represents the radioactive half-life of the radioisotope in question. The information relating to each emitted γ photon (emission position, disintegration time, initial energy and emission angle) is determined. The emitted γ photon then travels a certain distance in the matter before interacting. This distance depends on its energy, the density and the chemical composition of the material crossed. The length of the photon path in the material before interaction is calculated from the cumulative distribution function expressed by the probability of attenuation of a photon in the material. The probability density function $f(x)$ corresponding to the interaction of a photon between the distances x and $x + dx$ is:

$$f(x) = \mu \times e^{-\mu x} \quad (2.9)$$

where μ represents the attenuation coefficient of the material for the energy of the γ photon considered. Thus, the probability that a photon γ travels at least the distance d in the material is given by:

$$F(d) = \int_0^d \mu e^{-\mu x} dx = 1 - e^{-\mu d} \quad (2.10)$$

Drawing a random number $R = 1 - e^{-x}$ and then inverting the cumulative distribution function $F(d)$ defined in the preceding equation makes it possible to determine d such that:

$$d = -\frac{1}{\mu} \ln(1 - R) = -\lambda \ln(1 - R) \quad (2.11)$$

where λ represents the mean free path of the γ photon in the medium considered. If the γ photon crosses media of different densities, the distance d is calculated at each change of medium to consider the specific attenuation coefficients of each medium.

- At the energies used in nuclear medicine, the γ photon can interact in matter according to three types of interaction: the photoelectric effect, Compton scattering. The laws of probability

governing these different processes are well known. Thus, particle interactions in the material are described by cross-sections Interaction representing the probability that the particle will interact in the medium:

$$\mu = \mu_R + \mu_C + \mu_P \quad (2.12)$$

where P, C, R represent respectively the contributions of the photoelectric effects, Compton and Rayleigh. These coefficients are classified in tables by atomic element and physical effect. The type of interaction of the photon γ in the material is selected according to the drawing of a random number R uniformly distributed in the interval [0,1]:

If $R < P$: the photon γ interacts by photoelectric effect;

If $P < R < C$: the photon γ interacts by Compton effect;

Otherwise, the photon γ interacts by Rayleigh effect.

At each stage, the evolution of the particle is determined from the random draws. The particles are tracked until they come out of the simulation volume or according to the user defined shut-down conditions. These can be of two types: a minimum energy condition and or a minimum path condition from which particles are no longer tracked. The stopping conditions notably make it possible to optimize the calculation times. The γ photons interact in the detector, as a function of their energy and by photoelectric effect (absorption of the γ photon) or Compton. The γ photon is diffused and deviated from its initial trajectory, its energy after diffusion is obtained by the Compton diffusion. For Anger's cameras, the detector is most often made of a scintillating crystal of NaI(Tl). These interactions produce light photons that are transported to the photomultiplier tubes and then converted into a signal. The position of the interaction is calculated from the calculation of the barycenter of the positions of the photoelectric and Compton interactions, weighted by the energy deposited at each interaction. Finally, the energy response of the detector can be modeled, if necessary, by a Gaussian and which can then be defined by a width at half height. In addition to uncertainties related to the generation of random numbers, results from Monte Carlo calculations are also subject to statistical uncertainties. To avoid statistical fluctuations, it is necessary to simulate many photons. Uncertainty is determined by the following relation:

$$\delta = \frac{1}{\sqrt{N}} \sqrt{\frac{1-p}{p}} \quad (2.13)$$

with N: the number of binomial draws of expectation N_p There are mainly two types of Monte-Carlo codes used in nuclear medicine imaging: generic codes and so-called specific or dedicated codes.

2.3 Generic codes

Generic codes have been developed for simulation in nuclear physics or particle physics. The main codes currently available are shown below:

-EGS (Electron Gamma Shower) was developed in 1963 at the Stanford Linear Accelerator Center (SLAC, USA) [34] . This code makes it possible to simulate the transport of photons and electrons in an arbitrary geometry and for an energy range of a few keV to TeV. Several versions are available, the most recent being EGS5 [35] and EGSnrc [36]; the latter version has efficient section tables for low energy photons and allows a more precise simulation of the transport of charged particles.

- MCNP (Monte Carlo N-particle Transport Code) [37] was developed at Los Alamos National Laboratory (LANL, USA). This code was developed during the Manhattan Project during the Second World War. It makes it possible to simulate the transport of electrons, photons and neutrons, which makes it one of the simulation software programs most widely used by the scientific community.
- The MCNPX (Monte Carlo N-Particle eXtended) simulation code, also developed at LANL [38], simulates the transport of electrons, photons, neutrons and also heavy charged particles.
- PENELOPE (PENetration and Energy LOss of Positrons and Electrons in Matter) was developed at the University of Barcelona (Spain) [39, 40, 41]. This code makes it possible to simulate the transport of electrons, positrons and photons in simple and composite materials and for an energy range of a few hundred eV to 1 GeV.
- GEANT (GEometry ANd Tracking) is a tool developed at CERN (European Center for Nuclear Research, Switzerland) for particle physics experiments. The latest version of this currently available software is GEANT4 [42], coded in C++ and using object-oriented programming methods. These generic codes, widely documented because they are used by a large community of physicists, can nevertheless be difficult to implement in the case of more specific simulations because of their complexity. This is one of the reasons to explain the development of simulation codes dedicated to nuclear imaging.

2.4 The dedicated codes

Software dedicated to Monte Carlo simulations in nuclear medicine have been developed to meet the specific needs of this imaging modality. Many codes are usable in SPECT among which:

- SIMIND (Simulation of Imaging Nuclear Detectors) developed by Professor Ljungberg's team [43] at the University of Lund (Sweden) for SPECT related applications;
- SimSPECT (Simulation for SPECT), which is a Monte Carlo simulation code derived from the MCNP code and developed only for SPECT [44, 45];
- SIMSET (Simulation System for Emission Tomography) available since 1993 for SPECT and PET [45], this simulation software is regularly updated by the University of Washington;
- GATE (Geant4 Application for Emission Tomography), which was initiated in 2001. The OpenGATE collaboration, a group of laboratories, was created in 2002 to make available to the general public the first version of this software dedicated to imaging. in nuclear medicine and usable for SPECT and PET applications [46]. The latest version of this software (version 8.2) has new features that make it possible to perform Monte Carlo simulations for other applications: radiotherapy, dosimetry or tomodensitometry. Also, several bug corrections and update have been made. Among them:
 - adaptation to the new RTK 2.0 release
 - solved random crash
 - time is stored in double rather than float in Phase Space
 - optimization of Voxelized Mass.

Dedicated codes are certainly easier to use than generic codes but may have some disadvantages due to their lack of flexibility. They may also have limitations in terms of development and support because they are less well documented and used than generic codes.

2.5 Simind

The Monte Carlo simulation code, `simind`, describes a standard clinical SPECT camera, and it can easily be modified for all type of calculation or measurement in SPECT imaging. `simind` was written by fortran-90 is used for all operating systems (linux, MacOS, Windows), Monte carlo program facilitates the study of radiation transport, which helps to understand the causes of having degraded images, `simind` has been developed by Professor Michael Ljungberg (Medical Radiation Physics, Department of Clinical Sciences, Lund University, Sweden). `Simind` consists of two main programs named "`simind`" and "`change`", "`change`" allows the definition of the system to simulate and the creation of the output data, "`simind`" allows the simulation of input files created by "`change`" and displaying the results on the screen or on specific files. The desired imaging system is selected by the "`change`" program, which contains a series of menus, in which specific system parameters can be entered in a data file used by the "`simind`" program. we assume a base name for the saved file and a three-character extension "`smc`", so the output files keep the same base file name but with other extensions. when opening the program "`changes`" a file is created with the name "`simind.smc`", on this file all changes made by "`change`" will be saved, even when exporting data to `smc` files with unique names, the content of "`simind.smc`" will be updated. Thus, `simind.smc` should be considered as a temporary file. The coordinate system is defined in the figure below. when simulating SPECT, the camera

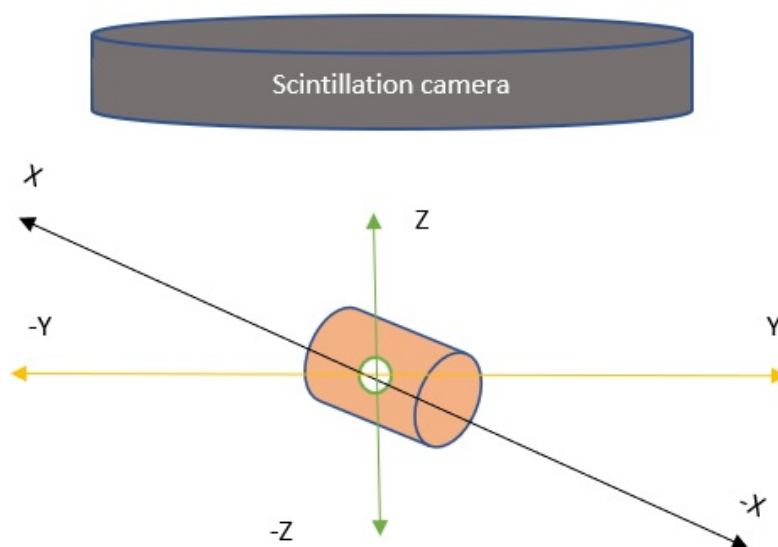


Figure 2.2: The coordinate system for `simind` program

rotates in the YZ plane. the first image of density / activity obtained is located towards + X and the last image towards -X. The diagram below describes the relationship between the program "`change`" and `simind` and the files used or produced in a simulation project.

The first page in the "`change`" program contains fifteen "main", which allows to define the general parameters of the simulation, such as the SPECT or planar image simulation mode, also showing the possible simulation indicators that can be used to control the simulation. the other pages contain ninety-nine "indexes" for specific parameters such as:

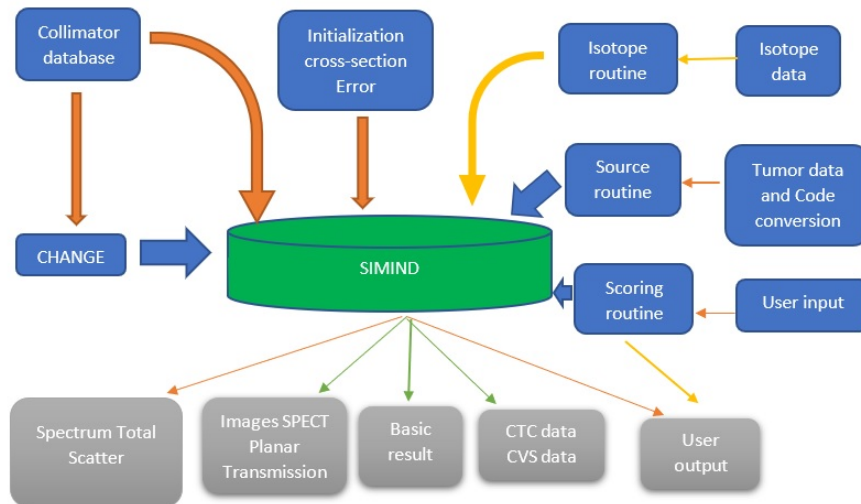


Figure 2.3: Simind program operation mode

- The camera scintillation parameters
- Non homogeneous phantom and SPECT parameters
- Collimator parameters
- Transmission simulation parameters
- Imaging parameters and other settings
- Solid state detectors settings

After the simulation of the file of extension smc, one obtains several files of different extension, to have the image of projection obtained one opens the file of extension *.a00 with the program imageJ, here is an example of image obtained by imageJ . simind is a SPECT virtual

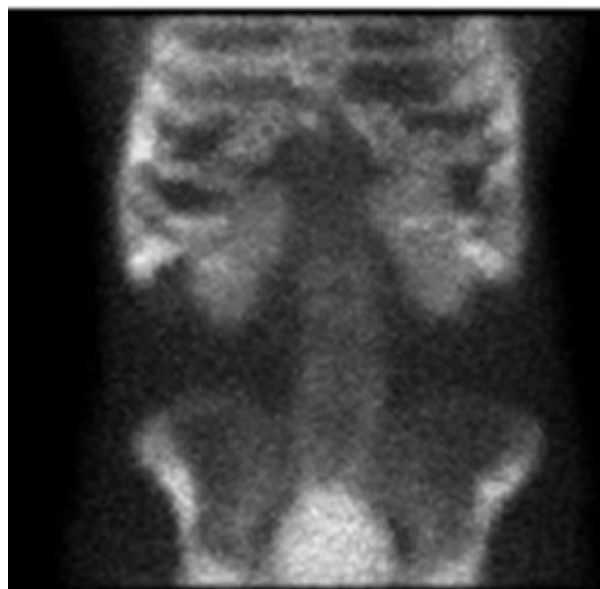


Figure 2.4: virtual Phantom MDP

camera, it gives projection images, in some cases we must optimize the results, it requires the reconstruction of image files.

here is an image obtained after the tomographic reconstruction of a projection file of the Zubal phantom based on voxel with Smc2castor (figure 2.5).

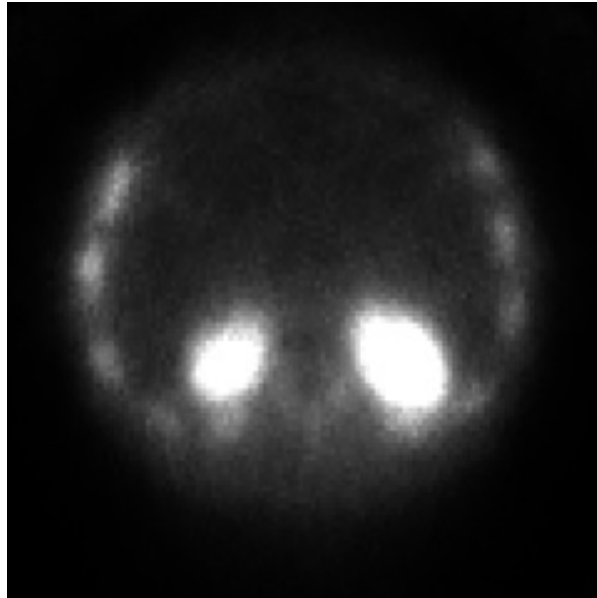


Figure 2.5: image obtained after the tomographic reconstruction

2.6 SPECT tomographic reconstruction methods

2.6.1 Principle

The single photon emission computed tomography allows to know the distribution of the radioactivity in the three dimensions of the space. During a tomographic acquisition, the acquisition heads are rotated around the subject. Several dozens of images are successively acquired, each from a different angle (we speak of projections). The images obtained on the projections depend on the distribution of the tracer in the body. Conversely, we want to know, knowing the projected images, what is the distribution of the tracer. The simplest method is to "back-project" the activity measured in each point of the projections in the direction from which it comes. In other words, the rear projection consists of filling all the pixels that are on the ray path with a value equal to the value in the pixel of the projection from which it started. Where the backprojected beams intersect is the source of activity, and activities are added (Figure 2.6). Backprojecting creates artifacts that have to be removed by applying image filtering techniques and by increasing the number of projections: an infinite number of projections is theoretically required to reconstruct perfectly a similar image to the object. In practice, at least 60 projections are used.

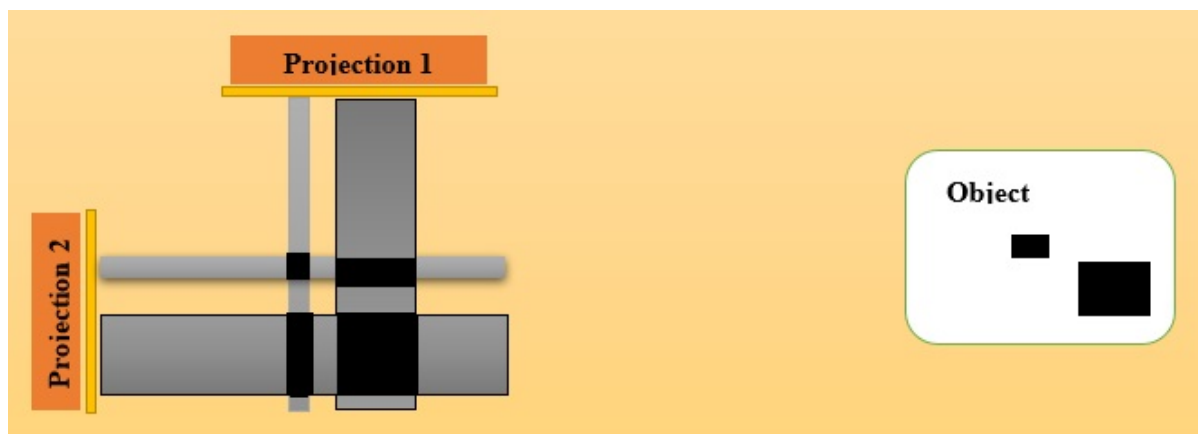


Figure 2.6: Reconstruction of an object with multiple structures

2.6.2 Analytical Methods: Filtered Projection (RPF) Back Projection

One of the first methods used in the clinic is rear projection of filtered projections [47]; until recently, this method was the most common. Each projection is divided into several pixels. Each pixel is associated with the measured activity: an integer value that can vary from 0 to several thousand detected hits. The activity of each of the pixels of all the projections is retroprojected. If the activity is intense in a pixel, the corresponding retro-projected ray is also of high intensity. Each projection is successively retroprojected and its values are added to the image being reconstructed. Filtered retroprojection algorithms have the advantage of being fast and easy to implement; However, they have the disadvantage of not being able to completely eliminate the reconstruction artifacts that can sometimes be troublesome [48].

2.6.3 Iterative methods

Another technique of tomographic reconstruction, iterative reconstruction, consists in linking many cycles of projections and retroprojections from an initial estimated image. The process is stopped when the reconstructed image gives projections like the measured projections. Conventional iterative methods use optimization algorithms such as maximum likelihood. This type of method was introduced by Shepp and Vardi, in 1982 [49], and then improved in terms of speed by OSEM (Ordered Subset Expectation Maximum) algorithms [50], and more recently by other methods such as that proposed by LEE [51]. Iterative reconstruction methods are increasingly used clinically because they provide better reconstructed images[53].

2.7 Methods for correcting scintigraphic images

2.7.1 Correction of attenuations

The attenuation of the photons considerably degrades the quality of the SPECT images by introducing artifacts and distortions of the image. The most important factor that degrades the resolution of images is the sick camera distance. The second important factor is due to the "self" absorption inside the patient. Tc-99m, for example, has a half-attenuation layer (ADC) of approximately 4cm in the soft tissues. This means that the deeper the organ that is explored,

the less the number of broadcasts reaching the camera is important. These "self" attenuation losses must be corrected during the reconstruction of the image [54, 55, 56]. For single- and double-headed gamma cameras, only soft correction can be made using generally the Sorensen or Chang methods [57, 58]. Indeed, the method of Chang [59] makes it possible to correct the effect of the attenuation from already reconstructed data: it is a post-correction. This is the method most commonly used and available on many clinical equipment. This method consists of:

Estimate, based on a mapping of the attenuation coefficients, the average attenuation undergone at each point of the image.

2.7.2 Fixed resolution loss with depth

It is certain that the spatial resolution decreases as the source - detector distance increases. This gives a point source a Gaussian image. The farther away the source is from the detector, the more Gaussian flattened (Figure 2.7). The correction method commonly used consists in

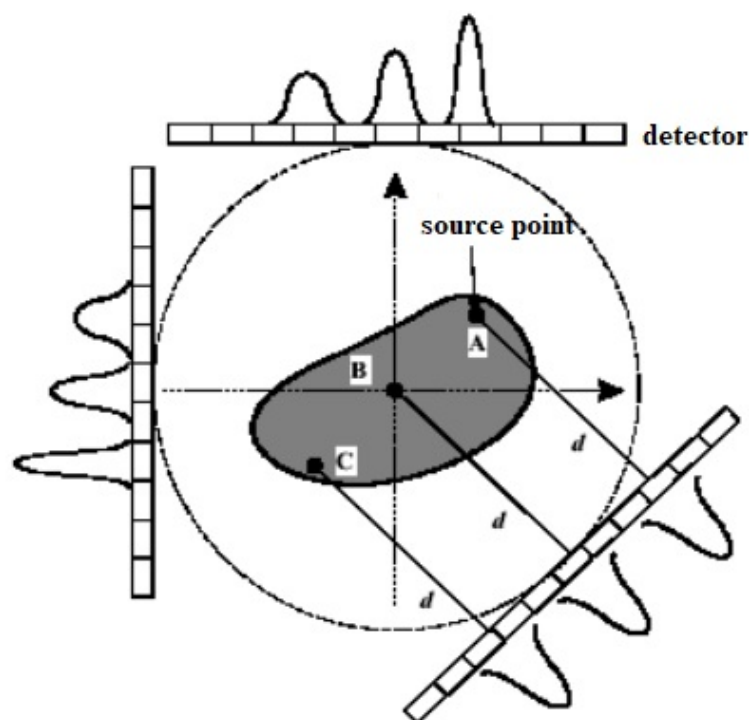


Figure 2.7: spatial resolution of the source - detector distance

modeling the resolution loss with the depth in the projection and rear projection operators at each iteration during the reconstruction for the iterative methods [60, 61, 62].

2.7.3 Elimination of photons in acquired projections

The spectrum of a gamma source is the superposition of a Compton scattering spectrum and a photoelectric peak. The presence of these scattering photons can not be fully corrected by the spectrometry of the detector and the collimator of the Gamma camera. Thus, the scattered radiation causes significant errors and detrimental to the quantification. The limited energy

resolution of SPECT systems causes difficulty in discerning and therefore rejecting the primary and scattered photons detected in the main acquisition window. The most traditional and easy-to-implement technique consists in estimating the proportion of photons diffused in the main window by several photons recorded in one or more spectrometric windows disjoined from the main window.

2.7.4 Triple energy window

This approach developed by Ogawa [63] (also called TEW for Triple Energy Window) consists in estimating the number of photons scattered by two narrow windows located on both sides of the main acquisition window with an overlap of the secondary windows and the principal window. Linear interpolation is used to determine the number of scattered photons in the main window (hatched trapezoid in Figure 2.8):

$$I_{diff} = \frac{w_1}{2} \left(\frac{I_2}{w_2} + \frac{I_3}{w_3} \right) \quad (2.14)$$

where, I_2 and I_3 are the numbers of photons recorded in windows w_2 and w_3 . The number of primary photons is estimated by:

$$I_{prim} = I_1 - I_{diff} \quad (2.15)$$

In practice, acquisitions related to this method are difficult to implement because of the overlapping of windows and the difficulty of SPECT systems in managing this condition. Ichihara [64] proposed to shift the two secondary windows to make them contiguous to the main window without overlapping. The implementation of this approach is easy, but it remains sensitive

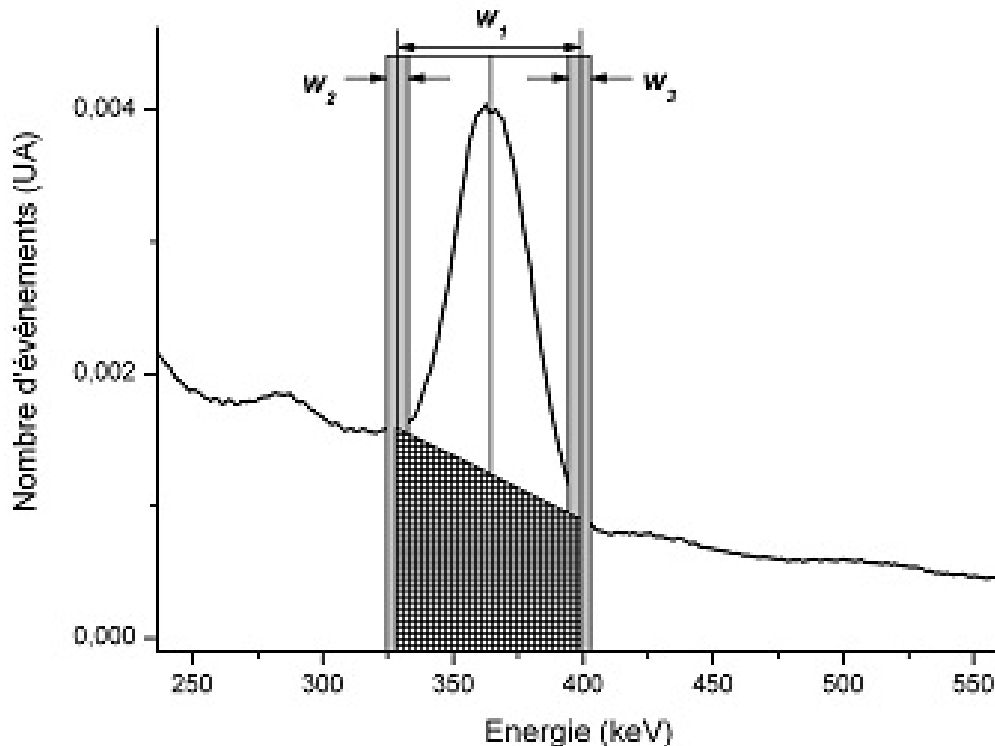


Figure 2.8: Principle of the triple subtraction method

to the position of the windows as well as their narrowness where few photons are detected thus increasing the noise in these data.

- Principle of the method of subtraction by triple window of the acquisitions where few photons are detected thus increasing the noise in these data. A filtering of the images obtained in these secondary windows was considered in order to limit the impact of the noise in the latter and showed better results of estimation of the diffused compared to the method where no filtering is envisaged [65]. In addition, the number of calculated broadcast events can be overestimated or underestimated because the broadcast events are not proportional to the width of the main window. Bong has recently proposed a variation of the triple window method, which partly makes it possible to overcome this problem with main windows not contiguous to the main window [66]. These different approaches of correction by subtraction have the disadvantage of modifying the structure of the noise of the projections before reconstruction and lead to a significant degradation of the signal-to-noise ratio when compared to additive methods [67].

2.7.5 Movement of the patient

Given the duration of certain categories of acquisition, the movement of the patient is an inevitable factor. This is a considerable problem in tomoscintigraphy. The alteration of the final image depends on:

- duration of the movement (> 13mn = quantitative abnormalities)
- kind of movement (Axial or Lateral)
- date of the movement (At the beginning, at the end or at mid-acquisition)
- type of camera (single head, double head or triple head)

There are several methods of calculating motion, the most used in myocardial scintigraphy is the tracing of the sinogram. Indeed, if we sum the lines of each projection on the cardiac zone, we obtain a series of unidimensional profiles making it possible to calculate the horizontal displacement of the heart from one projection to another, to specify the deviation from the theoretical sinusoid and to apply a possible correction [56, 68]

2.7.6 Conclusion

In this chapter different factors limiting the quality of the scintigraphic image are exposed and discussed. In the world of medical imaging, scintigraphy is an important diagnostic technique. Indeed, despite the weaknesses in the quality of the images, it permits an exploration of the functionality of anatomical structures. Improvements in the performance of the technique are envisaged on several levels. The methods, which seek to compensate for the effects of the image-degrading physical phenomena of attenuation, scattering, and variability of the detector's spatial response, are necessary to provide quantitatively accurate images. The acquisition systems, too, continue to multiply with the appearance of new interface cards and new acquisition and processing software.

Chapter 3

Contributions of the Monte Carlo study for optimization of medical imaging

Introduction

Nuclear Medicine is defined as bringing together all the techniques using radioelements in humans, whether for diagnostic or therapeutic purposes. The use of radioisotopes in medicine and appropriate detection equipment of many explorations of the functioning of human organs have been made possible. These techniques have made it possible to better understand the living and to treat it better. They have made available to biologists and nuclear physician's extraordinary diagnostic tools that radiology techniques could not provide. The choice of the radionuclide has a key role in nuclear medicine which appearing the lowest scatter fraction. the choice of the acquisition energy window is not trivial, due to the continuous and broad energy distribution of the bremsstrahlung photons. In addition, the presence of penetrated and scattered photons from collimator in single photon emission computed tomography images degrade resolution and contrast. Thus, image quality depends on sensitivity and resolution of the collimator -detector system. In this study, a Monte Carlo simulation SIMIND Code was used to investigate the effects of the energy windows, using a different collimator on the image contrast and contrast to noise ratio (CNR), in order to optimize different isotopes in single photon emission computed tomography (SPECT) imaging.

3.1 Contrast optimization for Y-90 SPECT imaging

3.1.1 Introduction

In gamma camera imaging, the acquisition energy window is centered around photopeak to detect majority of primary photons. However, for yttrium-90 (Y-90) bremsstrahlung, as the acquired spectrum is complex and continuous, the choice of acquisition energy windows is one of the most challenging topics in nuclear medicine.[85] Several works have been performed in the objective to optimize bremsstrahlung imaging.[85, 86, 87, 88, 89] However, no study has evaluated the image quality and accurate activity quantification for Y-90 bremsstrahlung in terms of contrast and contrast to noise ratio and also geometric, penetration, and scatter components. In this study, a Monte Carlo simulation SIMIND code [90] was used to investigate

the effects of the energy windows, using a high-energy (HE) collimator on the image contrast and signal to noise ratio (CNR), in order to optimize the Y-90 bremsstrahlung single-photon emission computed tomography (SPECT) imaging. The simulations were set up in such a way that it provides geometric, penetration, and scatter components to a separate file. At the end of simulations, binary images were imported in ImageJ software (Version 1.51) National Institutes of Health and the Laboratory for Optical and Computational Instrumentation (LOCI, University of Wisconsin).[91]

3.1.2 Materials and Methods

We simulated the Siemens Medical System Symbia equipped with a HE collimator and with detector having the following characteristics: 0.95 cm NaI (Tl) crystal thickness, 50 cm × 50 cm of area, intrinsic spatial resolution of 0.360 cm, and energy resolution of 10% at 140 keV. The collimator data used during the simulation are given in [Table 3.1]. Bremsstrahlung energy

Collimator	Diameter(cm)	Septa(cm)	Lenght(cm)	Hole shape	Col type
HE	0.400	0.200	5.970	Hexagonal	Parallel hole

Table 3.1: Collimator specifications

spectra were generated with SIMIND Monte Carlo code (version 6.1) by simulating six spheres of different sizes filled with Y-90 and located inside water cylindrical phantom (L: 10 cm, rayon 1: 11 cm, and rayon 2: 12 cm). The inner diameters of the six spheres used are: 3.7, 2.8, 2.2, 1.7, 1.3, and 1 mm. The activity concentration for the six spheres was 3.374 MBq/mL. The phantom was positioned at 15 cm from the detector surface. The projections were generated in matrices of 256 × 256 pixels, 0.24 cm pixel size, 128 views, and 360 ° clockwise gantry rotation. The simulation is done, starting with large acquisition windows [Table 3.2]. In order to refine the results, narrower acquisition windows were considered [Table 3.3].

Contrast and CNR were calculated by the following formulas:

	1	2	3	4	5
Subwindow (keV)	30-100	100-170	170-240	240-310	310-380
Center (keV)	65	135	205	275	345

Table 3.2: Size and central position for the sub-windows of the large window-set

	1	2	3	4	5
Subwindow (keV)	60-90	90-120	120-150	150-180	180-210
Center (keV)	75	105	135	165	195

Table 3.3: Size and central position for the sub-windows of the narrow window-set

$$Contrast = \frac{C_s}{C_b} - 1 \quad (3.1)$$

$$CNR = (C_s - C_b) \times \frac{V_{oxel}}{\sqrt{\sigma_s^2 + \sigma_b^2}} \quad (3.2)$$

$C_s = C_S/V_S$: Number of counts in the lesion (spheres) per voxel

S_C : Total counts in the lesion

V_S : Lesion volume in number of voxels

$C_b = N_C/V_B$: number of counts in the background compartment per voxel

N_C : Total counts in the background compartment

V_B : Background volume in number of voxels

σ_s : The variance in sphere

σ_b : The variance in background

3.1.3 Results

Figure 3.1 shows the energy spectrum as a function of energy for Y-90.

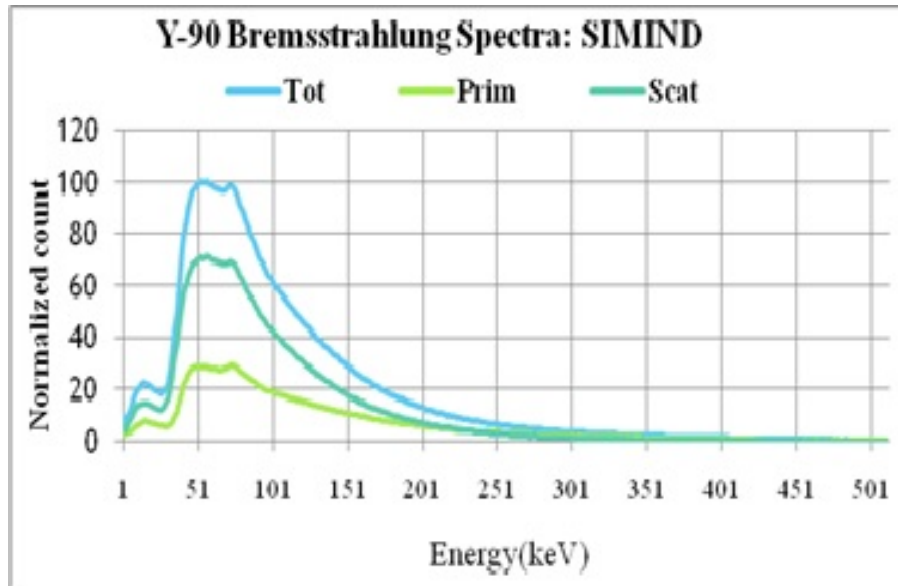


Figure 3.1: Monte Carlo simulated spectrum for yttrium-90[105]

As shown in Figure 3.2, the geometric component rehearses a high value in 135 keV for 1st acquisition and 130 keV in the second. Whereas, the scatter and penetration components are small at this energy in both cases[105].

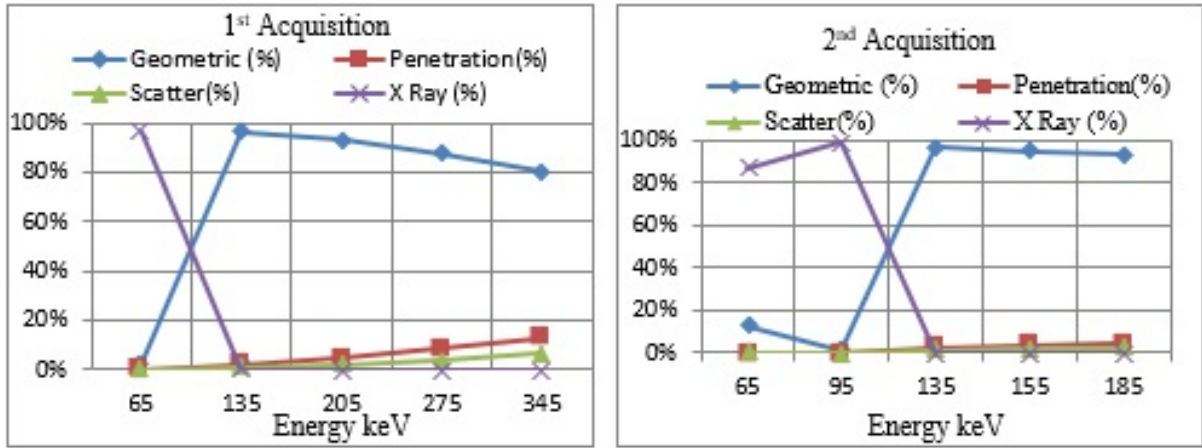


Figure 3.2: Contributions of geometric, penetration, scatter, and X-rays components with energy windows[105]

Figure 3.3 shows the effects of the energy window on the image contrast of the hot spheres with HE collimator. In comparison, both energy windows centered at 135 keV for 1st and 2nd acquisition provide a higher contrast than the others[105].

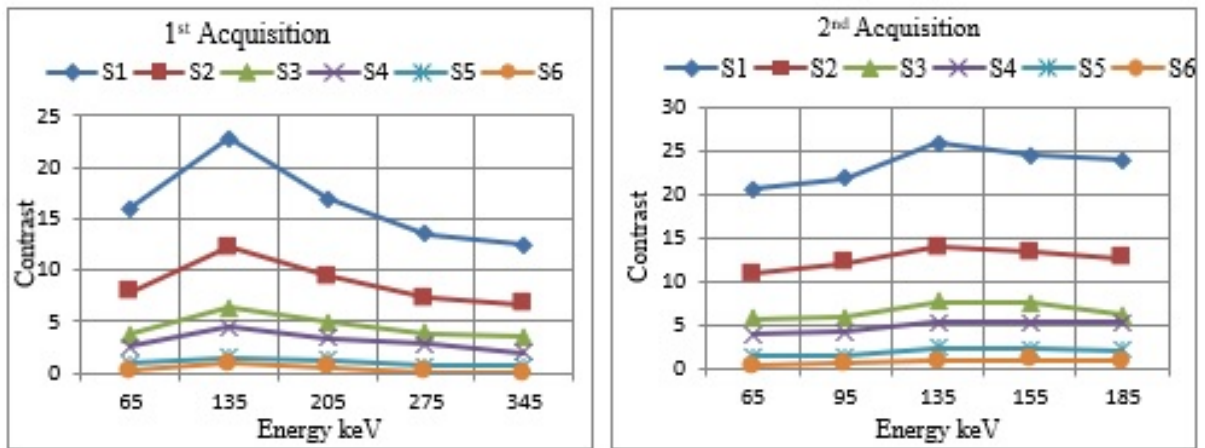


Figure 3.3: Contrast of the six spheres with energy window

Figure 3.4 shows the effect of energy windows on the image quality of the simulated Jaszczak phantom with six hot spheres.

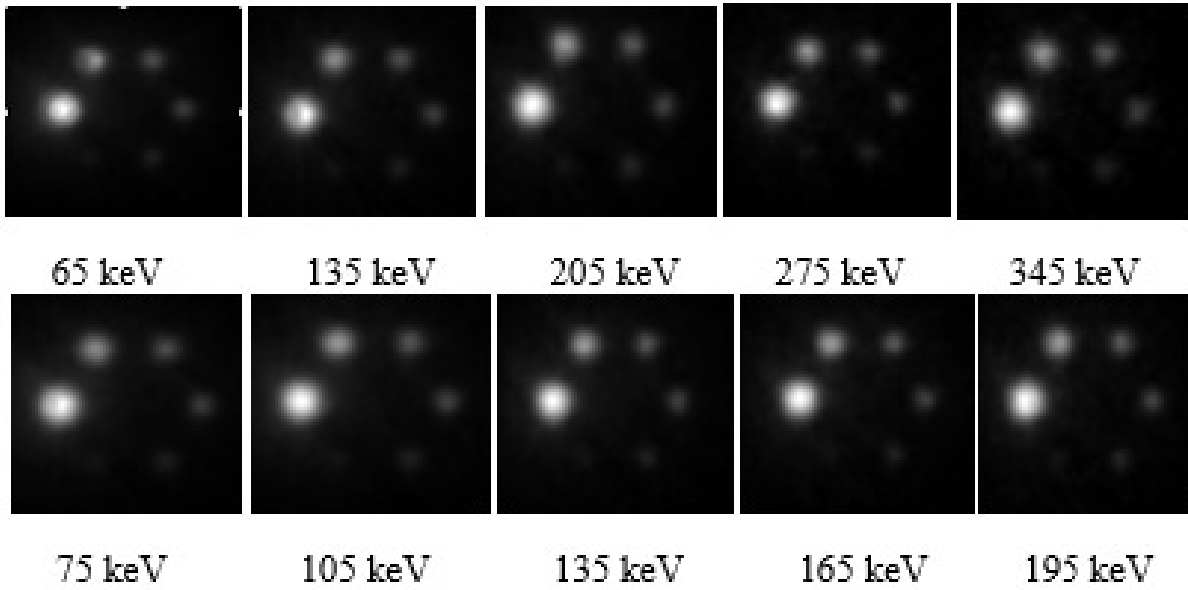


Figure 3.4: Images of simulated Jaszczak phantom with a high-energy collimator using large energy windows (above) and narrow energy windows (below)

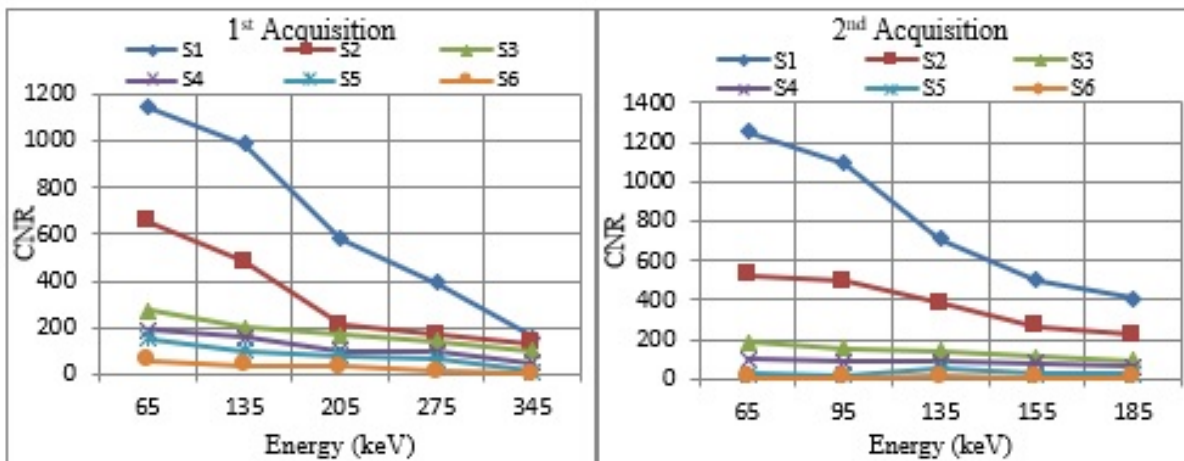


Figure 3.5: CNR of the six spheres

We notice, as shown in figure 3.5, that when the energy increases, the CNR decreases, and therefore, the image quality decreases. We observed the best CNR values for the first two energy windows in both acquisitions. In these windows, we can distinguish the two large spheres very well, but it is hard to distinguish the three smallest spheres. This seems to have been caused by increased background noise due to large penetration[105].

3.2 Determination of the Energy Windows for the TEW Scatter Correction Method in Gd-159 SPECT Using Monte Carlo Simulation

3.2.1 Introduction

In gamma camera imaging, the detection of Compton scattered photons within the photo-peak energy window depends on various factors, such as source distribution, object size, energy window settings, and source energies [69, 70, 71, 72, 104, 105, 106, 107, 108]. On the other hand, the removal of scattered photons is important in improving the quality and quantity of image [73, 106] because only primary photons provide correct spatial information regarding radioisotope distribution [74]. Diverse methods have been proposed to eliminate scattered photons from planar or reconstructed images, namely dual-energy window (DEW) [75], triple-energy window (TEW) [76, 106], photopeak window [77], downscatter correction [77], and combined scatter correction. Some other methods for this purpose include deconvolution [78], energy-weighted acquisition [79], iterative peak-erosion algorithm, spectral-fitting algorithm [80], factor analysis [81], inverse Monte Carlo reconstruction algorithm [82], and asymmetric photopeak window (offset high) [83]. The Gadolinium-159 (Gd-159) isotope can be used for nuclear medicine due to its half-life (18.5 h), in addition to beta (1001 keV) and gamma (main energy of 363.54 keV) emissions [84, 85]. In order to enhance the activity quantification and image quality for Gd-159 using the gamma emission of 365.54 keV, it is important to correct the scatter events caused by the photons scattered in the object. These photons produce errors regarding the decay location. This study aimed to estimate the contribution of scattered photons inside the main energy window in the TEW method which is known as a simple and practical technique. In the TEW method, two sub-windows were placed on both sides of the main photo-peak window. The primary count of photons in the photo-peak was calculated using the counts acquired from the two adjacent narrow windows. The current study involved the comparison of the true primary to total ratio and primary to total ratio (estimated by TEW) using the SIMIND Monte Carlo simulation code [85]. The results could be beneficial

3.2.2 Materials and Methods

The SIMIND Monte Carlo code (version 6.1) was used to simulate the Siemens Symbia Medical gamma camera with high-energy (HE) collimators that have parallel holes (Table 3.4). The dimensions of the detector surface were 59.1×44.5 and had a NaI(Tl) crystal thickness of 2.54 cm. The detector was characterized by an intrinsic spatial resolution of 0.34 cm and energy resolution of 8.8% at 140 keV. The photons emitted toward the camera had an acceptance angle of 45° . The pixel size in the simulated planar source images was 0.34 cm with a matrix size of 128×128 cm. The binary images were imported to the ImageJ software developed by SIMIND.

We simulated a cylindrical water phantom (16 cm in diameter and 32 cm in height) positioned at a distance of 15 cm from the detector surface. Point sources with a diameter of 1 mm, filled with Gd-159 (3.7 MBq), were simulated at seven locations, including the center of the cylinder phantom, as well as offsets at 7 cm of X, Y, and Z directions relative to the center. Figure 3.6 depicts the geometry of the SPECT system and phantom used in this study. The main energy window was determined at the widths of 10%, 15%, and 20%, while centered at

	High-energy (HE) collimator
Hole geometric	Hexagonal
Hole length (cm)	5.97
Septal thickness (cm).	0.2
Hole diameter (cm)	0.4

Table 3.4: Characteristics of the Siemens Symbia medical system collimator

363 keV and the sub-energy window widths of 3 and 6 keV. The true primary to total ratio (P/T) was compared with the primary to total ratio estimated using TEW scatter-correction method with triangular approximation[106].

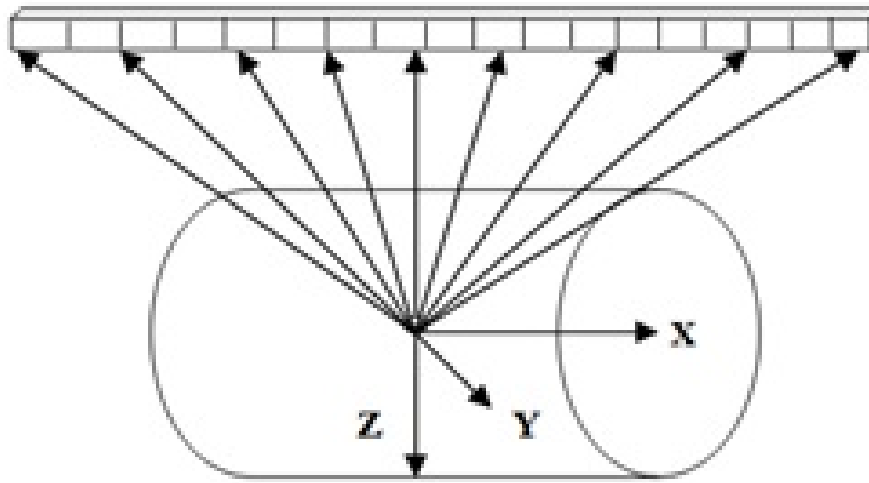


Figure 3.6: Geometry of the single photon emission computed tomography system and phantom

The count of primary photons for photopeak was estimated with the main window centered at the photopeak energy window and the two sub-windows on the sides of the main window. The following equation was used to estimate the scatter counts:

$$C_{sca} = \left(\frac{C_{left}}{W_s} + \frac{C_{right}}{W_s} \right) \times \frac{W_m}{2} \quad (3.3)$$

$$C_p = C_{tot} - C_{sca} \quad (3.4)$$

Where, C_{left} denotes the counts in left lower sub-energy window, C_{right} represents the counts in right lower sub-energy window, W_s is the width of sub-energy window, W_m refers to the width of main window, C_{tot} signifies the counts in main window, C_{sca} is the scatter counts, and C_p represents the primary counts. In addition, the primary to total ratio was calculated as:

$$P/T = \frac{C_p}{C_{tot}} \times 100 \quad (3.5)$$

3.2.3 Results

Tables 3.5 and 3.6 show the difference between the true primary to total ratio (%) and the estimated primary to total ratio at each position for 3 and 6 keV sub-windows. The primary to total ratio of photons depended on the source location and energy windows[106]

Subwin (3 keV)	10%		15%		20%		10%	20%	15%
Source position	P/T (TEW)	P/T (True)	P/T (TEW)	P/T (True)	P/T (TEW)	P/T (True)	Difference(%)		
(0, 0, 0)	88.05	85.4	88.4	80.2	82.17	75.36	2.65	8.2	6.82
(-7, 0, 0)	90.34	84.2	84.43	79.3	80.25	74.11	6.14	5.13	6.14
(7, 0, 0)	89.56	85.7	88.71	80.4	83.38	75.53	3.86	8.31	7.35
(0, -7, 0)	94.13	92.5	90.02	89.2	88.22	86.32	1.63	0.82	1.9
(0, 7, 0)	92.55	92.1	90.28	88.6	87.78	85.6	0.45	1.68	2.18
(0, 0, -7)	83.73	76.5	82.35	69.1	76.66	63.27	7.23	13.25	13.39
(0, 0,7)	93.79	97.4	91.88	96.5	92.57	95.19	-3.61	-4.62	-2.62

Table 3.5: Difference between the true primary to total ratio (%) and primary to total ratio estimated by triple-energy window scatter correction method for sub-window 3

Subwin (6 keV)	10%		15%		20%		10%	20%	15%
Source position	P/T (TEW)	P/T (True)	P/T (TEW)	P/T (True)	P/T (TEW)	P/T (True)	Difference(%)		
(0, 0, 0)	75.85	85.4	75.6	80.2	66.25	75.40	-9.55	-4.6	-9.15
(-7, 0, 0)	81.16	84.2	68.07	79.3	65.18	74.11	-3.04	-11.23	-8.92
(7, 0, 0)	77.57	85.7	76.12	80.4	66.32	75.53	-8.13	-4.28	-9.18
(0, -7, 0)	86.67	92.5	80.99	89.2	78.13	86.32	-5.83	-8.21	-8.17
(0, 7, 0)	84.63	92.1	81.65	88.6	76.03	85.6	-7.47	-6.95	-9.75
(0, 0, -7)	67.85	76.5	63.82	69.1	55.26	63.27	-8.66	-5.28	-8.04
(0, 0,7)	89.48	97.4	85.61	96.5	86.94	95.19	-7.92	-10.89	-8.26

Table 3.6: Difference between the true primary to total ratio (%) and primary to total ratio estimated by triple-energy window scatter correction method for sub-window 6[106]

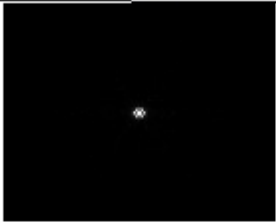
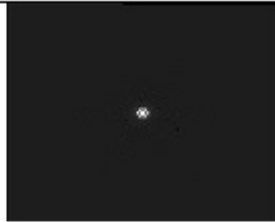

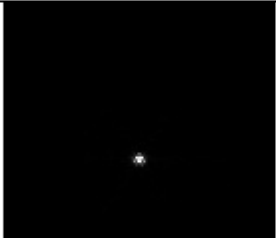




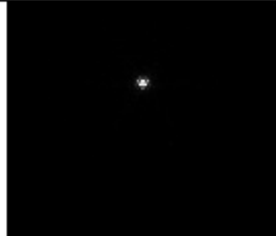









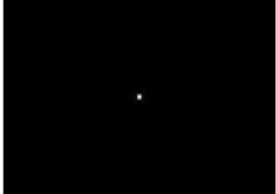


Source position (x, y, z)	True primary images	Primary images (TEW)	Total images
(0, 0, 0)			
(-7, 0, 0)			
(7, 0, 0)			
(0, -7, 0)			
(0, 7, 0)			
(0, 0, -7)			
(0, 0, 7)			

Figure 3.7: Gadolinium-159 point sources obtained for the sub-windows of 3 keV and a main energy window of 10%

In the current study, it was shown that the detected scattered photons within photo-peak energy window highly depended on the size of source distribution and energy window parameters. The use of SIMIND Monte Carlo simulation code facilitates tracking and recording the life history of the individual photon originating from the source. This allows the accurate calculation of the scattered photon fractions in different energy windows[105, 106, 107, 108]. The TEW scatter correction method was easily executed in the clinical trial.

3.3 Comparison of image quality of different radionuclides Tc-99m, Sm-153, and I-123

3.3.1 Introduction

In nuclear medicine, the radionuclides technetium-99 m (Tc-99 m) and iodine-123 (I-123) are most commonly used in single-photon emission computed tomography imaging. While, Samarium-153 (Sm-153) emits gamma radiation at 103 keV and has a physical half-life of 46.7 h, which is well suited for scintigraphic imaging.[92] Whereas, Sm-153 possesses both therapeutic beta and diagnostic gamma radiations, making it an alternative radionuclide to Y-90 in liver cancer treatment.[93] The Sm-153 imaging was useful in gastrointestinal scintigraphy.[93] In addition, Sm-153 has been used in various scintigraphic studies.[94, 95] Sm-153 has average, and maximum beta particle ranges in water of 0.5 mm and 3.0 mm, respectively. It is undeniable that the image quality strongly depends on the types of detected photons in the photopeak window. This photon reaching the detector were classified as: the geometric component (passed without any interaction inside the collimator), the penetration component (passed through septa without attenuation), or the scatter component (scattered in the septa). In addition, photons that are absorbed in the collimator septa produce an X-ray component by the photoelectric effect.[96] Only the first component provides the correct information. The penetration and scattering effects in collimator degrade contrast, resolution, and quantification. As well as, image quality and quantification accuracy are affected by these factors.[97] Gamma camera cannot classify the detected photons into geometric, penetrated, or scattered photons. To solve this difficulty, we used Monte Carlo simulation technique to assess the geometric, penetration, and scatter contribution inside the photopeak window.[98] Whereas there are few studies related with the assessment of geometric, penetration, and scatter components.[99, 100, 101, 102]. The aim of this study was to evaluate the image quality for each radionuclide. We model the Siemens Symbia medical system Gamma Camera, using Monte Carlo SIMIND code.[86, 87, 88] Moreover, evaluate the geometric, scattered, and septal penetration components. We also evaluate the resolution and sensitivity (Cps/MBq).

3.3.2 Materials and Methods

Images were acquired on a Siemens Medical System Symbia using both a medium-energy (ME), low-energy high resolution (LEHR), and ME collimators [Table 3.7]. I-123 was imaged with ME collimator, whereas Tc-99 m and Sm-153 were imaged with LEHR [Table 3.8]. Therefore, a point source has been placed at 12 cm from the detector surface and located in horizontal cylindrical water phantom of dimension 16 cm × 22 cm × 22 cm. We have modeled the detector with a radius equal to 25 cm having 2.54 cm NaI(Tl) crystal thickness. We made

the intrinsic spatial resolution of 0.34 cm and energy resolution of 8.80% at 140 keV. We have used, the SIMIND Monte Carlo code developed by Michael Ljungberg. Images were acquired

	Medium Energy (ME)	Low Energy High Resolution (LEHR)
Geometric of hole	hexagonal	hexagonal
Length of hole(mm)	4.064	2.405
Septal thickness(mm)	0.114	0.016
Diameter of hole(mm)	0.294	0.111

Table 3.7: Collimator specifications

Tc-99m		Sm-153		I-123	
Energy(keV)	Abundance(%)	Energy(keV)	Abundance(%)	Energy(keV)	Abundance(%)
20,67	1,12	40,9	16,6	27,2	24,69
21,02	0,18	41,54	30	27,47	45,98
140,51	88,5	47,11	9,45	31,1	13,16
-	-	48,38	2,44	31,76	2,86
-	-	48,38	2,44	31,76	2,86
-	-	75,42	0,17	346,35	0,13
-	-	83,37	0,19	440,02	0,42
-	-	89,49	0,16	505,33	0,27
-	-	97,43	0,77	528,96	1,28
-	-	103,18	29,19	538,54	0,38

Table 3.8: Energies and intensities of gamma rays emitted from: The technetium-99m, samarium-153, and iodine-123 sources

using a 128×128 matrix and a pixel size = $0.34 \text{ mm} \times 0.34 \text{ mm}$. The images created by SIMIND in ImageJ software, National Institutes of Health, and the Laboratory for Optical and Computational Instrumentation (University of Wisconsin).[91]

[Table 3.8] shows photons energies and intensities of I-123, Tc-99 m, and Sm-153 radionuclides decay. For I-123 and Sm-153, ten peaks have been simulated, and three peaks have also been simulated for Tc-99 m [Table 5.2]. Simulations were carried out for two separate conditions: in air and with scattering medium (cylinder of water). In this simulation study, the main energy window was centered on the main energy peak of radionuclides for width of 20% of this energy (I-123 [159 keV]: 143–175 keV, Tc-99 m [141 keV]: 131–151 keV, and Sm-153 [103 keV]: 93–113 keV). The point spread function (PSF) was studied for each radionuclide. The full width at half maximum (FWHM) and the full width at tenth maximum (FWTM) were computed from the PSF to quantify the resolution. All imaging parameters have been compared with or without a scattering medium.

3.3.3 Results and Discussion

The detected spectrum of radionuclides without collimator is shown in Figure 3.8. The energies are shown the energies of the main emission peaks of the isotopes.

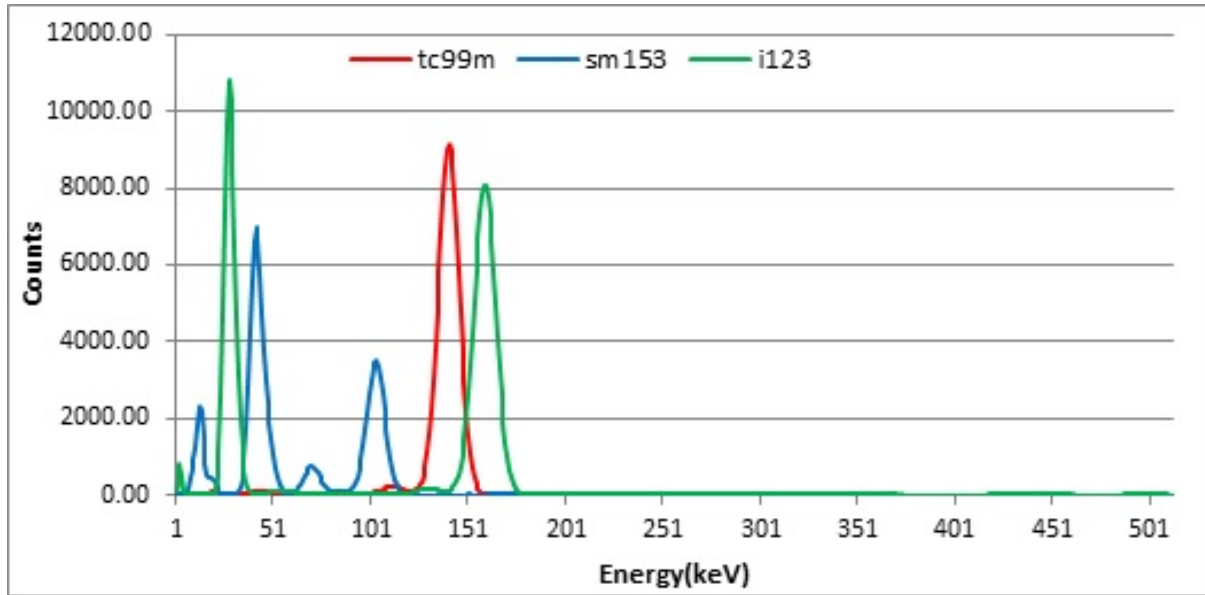


Figure 3.8: Energy spectra of photons on the detector without the use of collimator[101]

The different fractions detected within 20% peak energy window for all radionuclides are shown in [Table 3.9]. In water, the geometric fraction is large for Tc-99 m compared to the two other radionuclides. Whereas, in air this fraction, it is approximately the same for the three radionuclides. Because, these components depend on the energy of photons, object under study and collimator design parameters.

Phantom	Isotopes	Collimators	Geometric(%)	Penetration	Scatter(%)
Water	Tc-99m	LEHR	90.92	5.99	3.09
	Sm-153		85	10.46	4.36
	I-123	ME	88.08	7.4	4.52
Air	Tc-99m	LEHR	90.09	6.61	3.3
	Sm-153		89.49	7.13	3.24
	I-123	ME	90.43	6.03	3.54

Table 3.9: Geometric, penetration, and scatter fractions achieved with the isotopes

ME: Medium-energy, LEHR: Low-energy high resolution, Tc-99m: Technetium-99m, Sm-153: Samarium-153, I-123: Iodine-123

Figure 3.9 shows images of a point source for different radionuclides in water and air. The fogginess in the images formed by I-123 in water and air caused by scatter and penetration components due to high-energy gamma ray's emissions. The images formed by Sm-153 and TC-99 m show clearly a good quality[104].

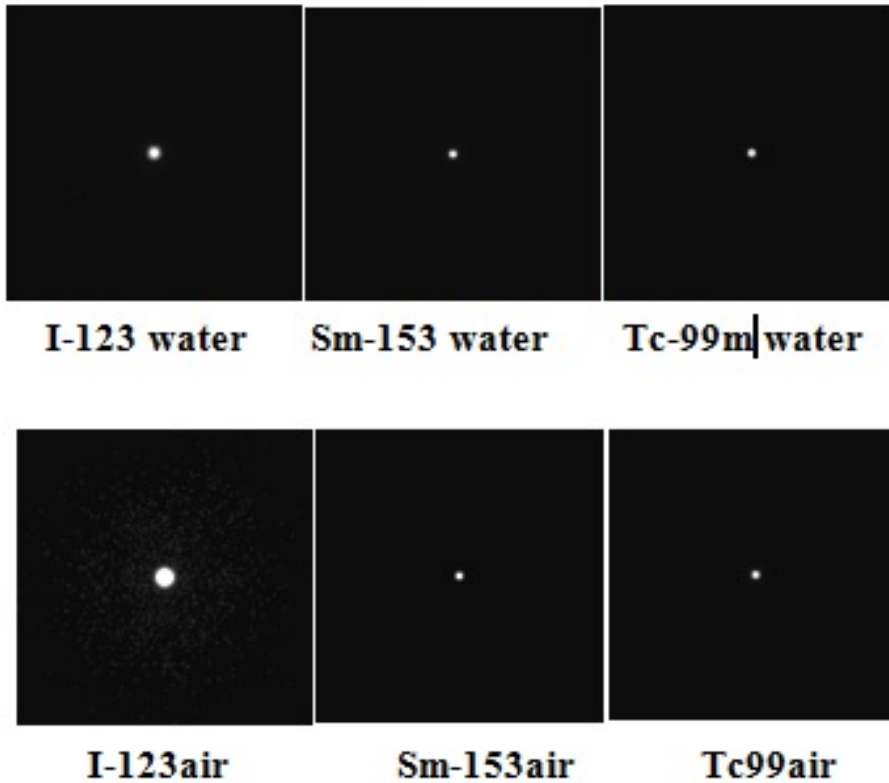


Figure 3.9: Planar images created at the end of each simulation

Resolution and sensitivity (Cps/MBq) study The PSF obtained for all of the isotopes, in air and water, are shown in [Figure 3.10]. Tc-99m and Sm-153 offer a better resolution than the I-123 in both cases. The curve of I-123 with the ME collimator shows the effects of the septa which lowers the resolution.

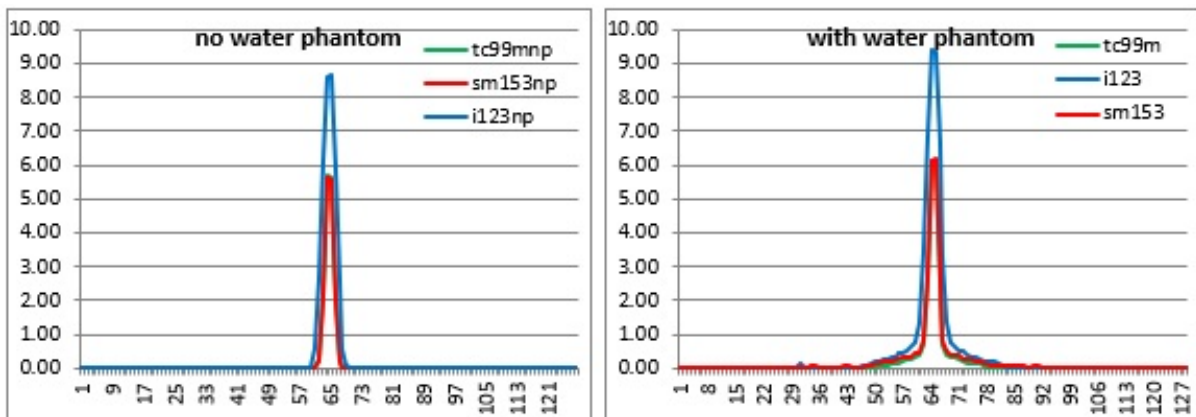


Figure 3.10: Point spread function for technetium-99 m, Samarium-153, and Iodine-123

Images quality depends on resolution and by sensitivity of the detector collimator system. [Figure 3.11] shows the comparison of sensitivity for three radionuclides.

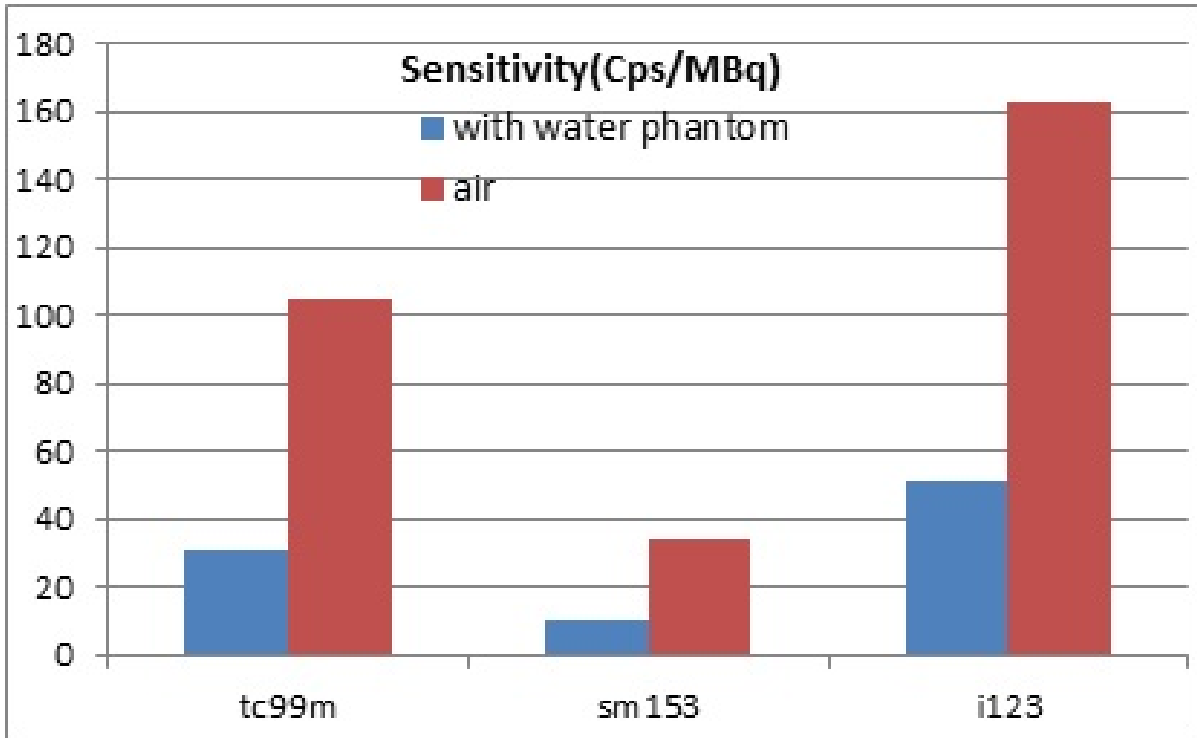


Figure 3.11: Sensitivity at the end of simulation[104]

Figure 3.11 shows that for each isotope the water phantom decreases the sensitivity. For I-123, the ME produced the high sensitivity compared with LEHR for two other radionuclides.

Quantification of the resolution FWHM and FWTM were calculated from profiles through the source images. FWHM and FWTM are shown in [Table 3.10]; it shows that, for each isotope, the water phantom increases FWTM, while FWHM remains roughly the same. FWHM was better for the LEHR then for the ME collimator. In addition, FWHM was similar for both Tc-99 m and Sm-153.[104]

Phantom	Isotopes	Collimators	FWHM(mm)	FWTM(mm)	Sensitivity (cps/MBq)
Water	Tc-99m	LEHR	3,19	6.73	31.21
	Sm-153		3.22	7.39	10.16
	I-123	ME	4.89	9.89	51.22
Air	Tc-99m	LEHR	3.01	5.41	104.9
	Sm-153		3	5.39	34.48
	I-123	ME	4.62	7.78	162.7

Table 3.10: Full width at half maximum, full width at tenth maximum, and sensitivity data for the different radionuclides point source[104]

3.4 Conclusion

In Y-90 bremsstrahlung imaging, the image quality and quantification are limited due to the high levels of object scatter, collimator septal penetration, and collimator scatter. The parallel hole collimator and energy window optimization in Y-90 have been studied.[14, 15, 86, 87, 88, 89, 105] In this study, we used Monte Carlo simulation SIMIND code to demonstrate how the image quality degrades as function of imaging parameters[104, 105, 106, 107, 108]. We have evaluated the image quality considering the contrast and contrast to noise ratio (CNR). The simulation data indicates that the choice of the acquisition energy window for Y-90 imaging has a great effect on the image contrast and contrast to noise ratio. Figure 3.3 shows the high contrast values in 135 keV center for both acquisitions. We notice, as shown in Figure 3.5, that the best CNR values are obtained in the first three windows. The simulations also show that the penetration is a significant problem for HE collimator at HE. The HE collimator with an energy window between 120 and 150 keV was selected as optimal acquisition setting with consideration of the contrast and contrast to noise ratio (CNR) and geometric, penetration, and scatter photons. The optimization of collimator and acquisition energy window leads to improve the quantitative accuracy and Y-90 bremsstrahlung SPECT image quality. Gadolinium-159 as a beta emitter is an efficient radionuclide for cancer therapy [94, 95, 96, 97]. Therapeutic management requires quantitative imaging, which is difficult to perform due to several factors, such as object scatter. Previous studies on the properties of therapeutic and scintigraphic images with Gd-159 demonstrated that the images obtained with a high-energy general-purpose collimator possessed low quality [73, 85, 106, 107, 108]. The scatter correction methods are useful to improve the image quality and activity quantification. Noori-Asl et al. [85, 105, 106] evaluated and compared six scatter correction methods for SPECT Tc-99m spectrum using SIMIND Monte Carlo simulation. They introduced TEW method, considering triangular approximation, as the most proper correction procedure. However, there is no study regarding the fraction of Gd-159 scattered photons as the function of optimal main and sub-energy windows for the implementation of the TEW method. Selection of the optimal main and sub-energy windows is very important and can lead to suitable image quality. Therefore, the selection of the main and sub-energy windows was different in Gd-159 SPECT imaging. It is important to choose proper energy windows for avoiding the scattered photons that degrade quantification and image quality. As a result, the chosen main and sub-energy windows impose a great effect on scatter correction for Gd-159 SPECT imaging. Tc-99m and Sm-153 give the best and generally similar imaging properties with LEHR. For I-123, the ME collimator helps lowering the influence of high-energy gamma rays[104].

Conclusion

Nuclear medicine is characterized by its evolution over the course of history. The fastening development of technology in this domain appeals the interest of several researchers, either due to methods related to correcting acquisition system defects or due to methods' improvement of analysis to extract physiological parameters. Object scatter in radionuclide imaging is one of the major factors leading to image quality degradation. Therefore, the correction of scattered photons may have a great impact on improving the image quality. The purpose of this thesis work is to optimize the image acquired in nuclear medicine as well the simulation validation by the SIMIND Monte-carlo program, using quality parameters Contrast, CNR, FWHM.

The present study evaluated the TEW scatter correction method for Gd-159 imaging with SIMIND Monte Carlo simulation code. The obtained results showed that both 3 and 6 keV sub-windows with 10% main-energy window was optimum for implementing the TEW method. These findings might be helpful in the activity quantification of Gd-159. Moreover, the capacity of quantitative SPECT imaging was shown using the TEW scatter correction method. The results of this study shed light on Gd-159 radionuclide as a new privileged radionuclide in the treatment and diagnosis of cancer.

Moreover, the obtained results showed that the HE parallel-hole collimator with energy window 120–150 keV conditions provides the best imaging performance based on contrast and CNR values. The optimization of these parameters leads to improved treatment efficacy and Y-90 bremsstrahlung SPECT imaging.

The effect of penetrated and scattered photons has been studied both qualitatively and quantitatively for Sm-153 and Tc-99 m and I-123. Since the results of the simulation show that the Sm-153 and Tc-99 m produced, generally, the best and similar imaging characteristics with LEHR collimator. However, the sensitivity obtained, with air and water phantom, was more than that of the other one. For I-123 imaging, the use of an ME collimator is important when the resolution is not required[104].

Bibliography

- [1] Darcourt J (2007). «Médecine Nucléaire », V 31, N° 4, p.125.
- [2] AIEA and OMS.(1976). « Médecine nucléaire-Rapport d'un comité mixte AIEA/OMS d'experts de l'utilisation des rayonnements ionisants et des radio-isotopes à des fins médicales », p. 8.
- [3] Yarmonenko S P. (1988), Radiobiology of humans and animals. Mir. Publishers, Moscow, 341: 355.
- [4] Purohit R K., Tak S., Chakrawarti A. and Bhartiya K M. (2009),Protective role of Aloe Vera against radiation and cadmium induced histopathological changes in the liver of Swiss Albino mice. Pharmacologyonline 2: 595-604.
- [5] Borek C., Abraham S K. and Sarma L. (1993), Molecular mechanisms in cancer induction and prevention protective effects of chlorogenic acid, curcumin and beta-carotene against gamma radiation-induced in vivo chromosomal damage. Envir. Healt. Perspect., 101: 237 – 245.
- [6] Georgios K., Nikolaos K., Vassilios A. and Vassilios K.(2009), Brachytherapy for prostate cancer: A systematic review. Advances in Urology, (6):1–11.
- [7] Wall B F., Hart D.(1997),Revised radiation doses for typical x-ray examinations. The British Journal of Radiology 70: 437-439; (5,000 patient dose measurements from 375 hospitals).
- [8] Kyung-Hyun, Do.(2016),General Principles of Radiation Protection in Fields of Diagnostic Medical Exposure.” Journal of Korean Medical Science 31.Suppl 1.
- [9] Petrucci R H., Harwood W S.,and Herring F G.(2002), General Chemistry (8th ed., Prentice-Hall 2002), p.1025–26
- [10] Targholizadeh H., Raisali G., Amir R., Jalilian., Nima R., Mohammadreza E., Mohsen K.and Dehghan.(2010), Cyclotron production of technetium radionuclides using a natural metallic molybdenum thick target and consequent preparation of [Tc]-BRIDA as a radio-labelled kit sample. Nukleonika. 55(1): p. 113-118.
- [11] Bobeica M., Niculae D., Balabanski D, Filipescu D, Gheorghe I, Ghita D.G. and Luo W.(2016), Radioisotope Production for Medical Applications at ELI-NP, Romanian Reports in Physics, Vol. 68, Supplement, P. S847–S883.

- [12] Gopal B S. (2003), Internal Radiation Dosimetry Fundamentals of Nuclear Pharmacy. Fifth Edition.
- [13] Larsson A, (2005): "Corrections for improved quantitative accuracy in SPECT and planar scintigraphic imaging. Department of Radiation Sciences". Radiation Physics Umeå University, Sweden:p.22.
- [14] Rong X, Du Y, Ljungberg M, Rault E, Vandenberghe S, Frey EC, et al. Development and evaluation of an improved quantitative (90)Y bremsstrahlung SPECT method. Med Phys 2012;39:2346-58.
- [15] Heard S, Flux GD, Guy MJ, Ott RJ. Monte Carlo simulation of 90Y bremsstrahlung imaging. IEEE Nucl Sci Symp 2004;3579-83.
- [16] Rong X, Du Y, Frey EC. A method for energy window optimization for quantitative tasks that includes the effects of model-mismatch on bias: Application to Y-90 bremsstrahlung SPECT imaging. Phys Med Biol 2012;57:3711-25.
- [17] Frontera M., Aaron B., Tomas E., Mathilde F., Karin G., Martin O., Charlie S., Erik S., Julie Woodland, Peter Z., Uno Z.(2014), Future Supply Options of 99Mo and 99mTc, Mo-99 . Topical meeting on molybdenum-99 technological development, June 24-27.
- [18] Celler A., Hou X., Bénard F., Ruth T. (2011), Theoretical modeling of yields for proton-induced reactions on natural and enriched molybdenum targets. Physics in Medicine and Biology. 56 (17): 5469–5484.
- [19] Moore P W.(1984), Technetium-99 in generator systems. Journal of Nuclear Medicine. 25 (4): 499–502. PMID 6100549.
- [20] Eckelman W C. (2009), Unparalleled Contribution of Technetium-99m to Medicine Over 5 Decades. JACC: Cardiovascular Imaging. 2 (3): 364–368. doi:10.1016/j.jcmg.2008.12.013.
- [21] Swiniarski R. (2002). «La médecine nucléaire », p.2.
- [22] Driol G.2008. « Imagerie par rayonnement Gamma Diffusé à haute sensibilité », p.21.
- [23] Gopal B. Saha.(2006). «Physics and Radiobiology of Nuclear Medicine », p.108
- [24] Vuillez JP. « Médecine nucléaire-gamma caméra et Caméra à positon », p.59-66.
- [25] Buvat I.(2002). « Les atouts et faiblesses des caméras TEP dédiées en TEP corps entier, TEP-CT, TEMP pour la quantification », p.4.
- [26] GaGlione R. (2005). « Electronique d'acquisition d'une gamma-caméra », p.11.
- [27] Metz C.E., Atkins F.B. and Beck R.N. (1980). The geometric transfer function component for scintillation camera collimators with straight parallel holes. Phys. Med. Biol. 25 : 1059-1070.
- [28] Knoll G.F. (1989). Radiation Detection and Measurement, 2nd Edition, John Wiley and Sons, New York reculation: 463-73.

- [29] Floyd C.E., Jaszczak R.J., Harris C.C. and Coleman R.E. (1984). Energy and spatial distribution of multiple order Compton scatter in SPECT: a Monte Carlo investigation. *Phys. Med. Biol.* 29: 1217-1230.
- [30] Esquerré J.P., Danet B. and Gantet P. (1996). Évolution des gamma-caméras. *Revue de l'Acomen* 2: 175-181.
- [31] Moretti J.L. and Roussi A. (1993). Contrôle de qualité des gamma-caméras planaires et tomographiques. *RBM* 15 : 375-85.
- [32] Rosenthal M.S., Cullom J., Hawkins W., Moore S.C., Tsui B.M.W. and Yester M. (1995). Quantitative SPECT Imaging: A review and recommendations by the Focus Committee of the Society of Nuclear Medicine Computer and Instrumentation Council. *J. Nucl. Med.* 36: 1489-1513.
- [33] Lehmer, D. J. 1948 The Jornada Branch of the Mogollon, University of Arizona Bulletin, Social Science Bulletin No. 17.
- [34] Bielajew AF, Hirayama H, Nelson WR, Rogers DWO (1994). "History, overview and recent improvements of EGS4." Report NRC-PIRS-0436.
- [35] Hirayama H, Namito Y, Bielajew AF, Wilderman SJ and Nelson WR (2010). "The EGS5 Code System." SLAC-R-730 and KEK Report 2005-8.
- [36] Kawrakow I, Mainegra-Hing E, Rogers DWO, Tessier F and Walters BRB (2011). "The EGSnrc Code System: Monte Carlo Simulation of Electron and Photon Transport." NRCC Report PIRS-701.
- [37] Briesmeister JF (2000). "MCNP - A general Monte Carlo N-Particule transport code, Version 4C." Los Alamos National Laboratory report LA-13709-M
- [38] Hendricks JS, McKinney GW, Waters LS, Roberts TL, Egdorf HW, Finch JP, Trelue HR, Pitcher EJ, Mayo DR, Swinhoe MT, Tobin SJ, Durkee JW (2004). "MCNPX". Los Alamos National Laboratory report LA-UR-04-0569.
- [39] Baro J, Sempau J, Fernandez-Varea JM and Salvat F (1995). "PENELOPE: an algorithm for Monte Carlo simulation of the penetration and energy loss of electrons and positrons in matter." *Nuclear Instruments and Methods in Physics Research Section B.* 100 31–46.
- [40] Sempau J, Acosta E, Baro J, Fernandez-Varea J M and Salvat F (1997). "An algorithm for Monte Carlo simulation of coupled electron-photon showers." *Nuclear Instruments and Methods in Physics Research Section B.* 132 377–90.
- [41] Salvat F, Fernandez-Varea J M, Baro J and Sempau J (1996). "PENELOPE, an algorithm and computer code for Monte Carlo simulation of electron-photon showers." Technical Report no 799
- [42] Agostinelli S, Allison J, Amako K, et al. (2003). "GEANT4 – a simulation toolkit." *Nuclear Instruments and Methods in Physics Research Section A.* 506:250-303.

- [43] Ljungberg M, Strand SE. (1989). "A Monte Carlo program for the simulation of scintillation camera characteristics." *Computer Methods and Programs in Biomedicine*. 29:257-72.
- [44] Yanch JC, Dobrzeniecki AB, Ramanathan C, Behrman R (1992). "Physically realistic Monte Carlo simulation of source, collimator and tomographic data acquisition for emission computed tomography." *Physics in Medicine and Biology*. 37:853-870.
- [45] Belanger MJ, Yanch JC, Lu A and Dobrzeniecki AB (1998). "The SimSPECT photon selector and multiple angular sampling of photons." *IEEE Nuclear Science Symposium Conference Record*. 3:2023-2025.
- [46] Harrison RL, Vannoy SD, Haynor DR, Gillipsie SB, Kaplan MS, Lewellen TK (1993). "Preliminary experience with the photon history generator module of a public domain simulation system for emission tomography." *IEEE Nuclear Science Symposium and Medical Imaging Conference*. 1154-1158.
- [47] Jan S, Santin G, Strul D, Staelens S, Assie K, Autret D, Avner S, Barbier R, Bardies M, Bloomfield PM, Brasse D, Breton V, Bruyndonckx P, Buvat I, Chatziioannou AF, Choi Y, Chung YH, Comtat C, Donnarieix D, Ferrer L, Glick SJ, Groiselle CJ, Guez D, Honore PF, Kerhoas-Cavata S, Kirov AS, Kohli V, Koole M, Krieguer M, van der Laan DJ, Lamare F, LARGERON G, Lartizien C, Lazaro D, Maas MC, Maigne L, Mayet F, Melot F, Merheb C, Pennacchio E, Perez J, Pietrzyk U, Rannou FR, Rey M, Schaart DR, Schmidlein CR, Simon L, Song TY, Vieira JM, Visvikis D, Van de Walle R, Wieers E, Morel C (2004). "GATE: a simulation toolkit for PET and SPECT." *Physics in Medicine and Biology*. 49:4543-4561.
- [48] Bracewell, R.N., and Riddle, A.C., 1967. Inversion of fan beam scans in radio astronomy. *Astrophysical J.*, 150, 427-434.
- [49] Drogmigny-Badin A. – «Fusion d'image par la théorie de l'évidence en vue d'applications médicales et industrielles», Thèse de doctorat : INSA Lyon, 1998.
- [50] Shepp L, Vardi Y (1982). "Maximum Likelihood Reconstruction for Emission Tomography." *IEEE Transactions on Medical Imaging*. 1:113-121.
- [51] Hudson HM, Larkin RS. (1994). "Accelerated Image-Reconstruction Using Ordered Subsets of Projection Data." *IEEE Transactions on Medical Imaging*. 13:601-609.
- [52] Lee S. J., «Ordered subsets Bayesian tomographic reconstruction using 2-D smoothing splines as priors», *Computer methods and programs in biomedicine*, 2003.vol.72, p27-42.
- [53] Mesina C.T, Boellaard R., Jongbloed G., Vander Vaart A.W, and Lammertsma A.A., «Experimental evaluation of iterative reconstruction versus filtered back projection for 3D [15O] water PET activation studies using statistical parametric mapping analysis», *NeuroImage*, 2003, vol.19, p.1170-1179

- [54] Buvat I., El Fakhri G., Péligrini M., Benali H., Todd-Pokropek A., and Di Paola R., «Importance respective des différentes corrections physiques en SPECT», *Revue de l'ACOMEN*, vol. 5, 1999, p. 169-179.
- [55] Rusinek H., «Clinical Spect Imaging: SPECT reconstruction techniques», edited by E. Kramer L. and Sanger J. J., Raven Press, 1995, p. 43-67.
- [56] Zanzonico P., «Clinical Spect Imaging Technical requirements for SPECT», *Instrumentation data acquisition and processing, and quality control*, edited by E.L. KRAMER and J. J. SANGER; Raven Press, 1995, p. 13-41 .
- [57] Buvat I., El Fakhri G., Péligrini M., Benali H., and Di Paola R., «Comparaison de différents protocoles de correction d'atténuation en imagerie cardiaque SPECT», *Revue de l'ACOMEN*, 1998, vol. 4, pp 121-129.
- [58] El Fakhri G., Buvat I., Benali H., Todd-Pokropek, A., and Paola R. Di, «Relative impact of scatter, collimator response, attenuation, and finite spatial resolution corrections in cardiac SPECT» *J. Nucl. Med.* Vol. 41, 2000, p 1400-1408.
- [59] Chang L.T., «Attenuation correction and incomplete projection in single photonemission computed tomography», *IEEE Tr. Nucl. Sci* , 1978, p.2780-2789.
- [60] Buvat I., El Fakhri G., Péligrini M., Benali H., Todd-Pokropek A., and Di Paola R., «Importance respective des différentes corrections physiques en SPECT», *Revue de l'ACOMEN*, vol. 5, 1999, p. 169-179
- [61] Kohli V., King M. A., Pan T. S., and VS. J. X, «Compensation for distance-dependent resolution in cardiac perfusion SPECT: Impact on uniformity of wall counts and wall thickness» *IEEE Trans. Nucl. Sci.* vol. 45, 1998, p.1104-1110.
- [62] Rusinek H., «Clinical Spect Imaging: SPECT reconstruction techniques», edited by E. Kramer L. and Sanger J. J., Raven Press, 1995, p. 43-67.
- [63] K. Ogawa, Y. Harata, T. Ichihara, A. Kubo, and S. Hashimoto. A practical method for position-depende Compton-scatter correction in single photon emission CT. *IEEE Trans Med Imaging*, 10 :408–12, 1991.
- [64] T. Ichihara, K. Ogawa, N. Motomura, A. Kubo, and S. Hashimoto. Compton scatter compensation using the triple-energy window method for single- and dual-isotope SPECT. *J Nucl Med*, 34 :2216–21, 1993.
- [65] M. A. King, D. J. deVries, T-S. Pan, P. H. Pretorius, and J. A. Case. An investigation of the filtering of TEW scatter estimates used to compensate for scatter with ordered subset reconstructions. *IEEE Trans Nucl Sci*, 44 :1140–5, 1997.
- [66] J-K. Bong, H-K. Son, J. D. Lee, and H-J. Kim. Improved scatter correction for SPECT images : a Monte Carlo study. *IEEE Trans Nucl Sci*, 52 :1263–70, 2005.

- [67] E. C. Frey, B. M. W. Tsui, and M. Ljungberg. A comparison of scatter compensation methods in SPECT : Substraction-based techniques versus iterative reconstruction with accurate modeling of the scatter response. In Proc IEEE Nuclear Science Symp Medical Imaging Conf, pages 1035–7, 1992.
- [68] Cochar G. M., « Notions de traitement et d’analyse d’image», Université de Picardie Jules Verne, 1998.
- [69] Ogawa K, Harata Y, Ichihara T, Kubo A, Hashimoto S. Estimation of scatter component in SPECT planar image using a Monte Carlo method. Jpn J Nucl Med. 1990; 27: 467-75.
- [70] Floyd CE, Jaszczak RJ, Harris CC, Coleman RE. Energy and spatial distribution of multiple order Compton scatter in SPECT: a Monte Carlo simulation. Phys Med Biol. 1984; 29:1217-30.
- [71] Floyd CE, Jaszczak RJ, Coleman RE. Inverse Monte Carlo: A Unified Reconstruction Algorithm for SPECT. IEEE Trans Nucl Sci.1985; 32: 779-85.
- [72] Sadremomtaz A, Telikani Z. Evaluation of the performance of parallel-hole collimator for high resolution small animal SPECT: A Monte Carlo study. Iran J Nucl Med. 2016; 24(2):136-43.
- [73] Razavi SH, Kalantari F, Bagheri M, Namiranian N, Nafisi-Moghadam R , Mardanshahi A, et al. Characterization of low, medium and high energy collimators for common isotopes in nuclear medicine: A Monte Carlo study. Iran J Nucl Med. 2017; 25(2):100-4.
- [74] Jaszczak RJ, Greer KL, Floyd CE Jr, Harris CC, Coleman RE. Improved SPECT quantification using compensation for scattered photons. J Nucl Med.1984; 25:893–900.
- [75] Ogawa K, Harata Y, Ichihara T, Kubo A, Hashimoto S. A practical method for position-dependent Compton-scatter correction in single photon emission CT. IEEE Trans. Med. Imaging. 1991; 10: 408.
- [76] Lagerburg V, de Nijs R, Holm S, Svarer C. A comparison of different energy window subtraction methods to correct for scatter and down scatter in I-123 SPECT imaging. Nucl Med Commun. 2012; 33(7):708-18.
- [77] Axelsson B, Msaki B, Israelsson A. Subtraction of Compton scattered photons in single-photon emission computerized tomography. J Nucl Med. 1984; 25: 490-4.
- [78] Hamill JJ, DeVito RP. Scatter reduction with energy weighted acquisition. IEEE Trans Nucl Sci.1989; 36: 1334-9.
- [79] Koral KF, Wang X, Rogers WL, Clinthorne NH, Wang X. SPECT Compton-scattering correction by analysis of energy spectra. J Nucl Med. 1988; 29: 195-202.
- [80] Gagnon D, Todd-Pokropek AE, Arsenault A, Dupras G. Introduction to holospectral imaging in nuclear medicine for scatter subtraction. IEEE Trans Med Imag. 1989; 8: 245-50.

- [81] Floyd CE, Jaszczak RJ, Coleman RE. Scatter detection in SPECT imaging: dependence on source depth, energy, and energy window. *Phys Med Biol.* 1988; 33:1075-81.
- [82] Koral KF, Clinthorne NH, Rogers WL. Improving emission-computed-tomography quantification by Compton-scatter rejection through offset window. *Nucl Inst and Methods in Phys Res A.* 1986; 242: 610-4.
- [83] Soares DCF, Menezes MA de BC, dos Santos RG, Ramaldes GA. Gd-159: preparation and preliminary evaluation as a potential antitumoral radionuclide. *J Radioanal Nucl Chem.* 2010; 284: 315-20.
- [84] Soares DCF, Sousa GFD, Barros ALBD, Cardoso VN, Oliveira MCD, Ramaldes GA. Scintigraphic imaging and increment in mice survival using theranostic liposomes based on Gadolinium-159. *J of Dru Del Science and Tech.* 2015; 30:7-14.
- [85] Lee YS, Kim JS, Kim KM, Lima SM, Kimb HJ. Determination of energy windows for the triple energy window scatter correction method in I-131
- [86] Roshan HR, Mahmoudian B, Gharepapagh E, Azarm A, Pirayesh Islamian J. Collimator and energy window optimization for 90Y bremsstrahlung SPECT imaging: A SIMIND Monte Carlo study. *Appl Radiat Isot* 2016;108:124-8.
- [87] Rong X, Frey EC. A collimator optimization method for quantitative imaging: Application to Y-90 bremsstrahlung SPECT. *Med Phys* 2013;40:082504.
- [88] Rong X, Ghaly M, Frey EC. Optimization of energy window for 90Y bremsstrahlung SPECT imaging for detection tasks using the ideal observer with model-mismatch. *Med Phys* 2013;40:062502.
- [89] Rong X, Du Y, Frey EC. A method for energy window optimization for quantitative tasks that includes the effects of model-mismatch on bias: Application to Y-90 bremsstrahlung SPECT imaging. *Phys Med Biol* 2012;57:3711-25.
- [90] Ljungberg M. The SIMIND Monte Carlo Program Home Page. Available from: <https://www.msf.lu.se/forskning/the-simind-monte-carlo-program>. [Last accessed on 2018 Oct].
- [91] Ferreira T, Rasband W. Image J Program. Available from: <https://www.imagej.nih.gov/ij/download.html>. [Last accessed on 2018 Oct].
- [92] Tse JW, Wiebe LI, Noujaim AA. High specific activity [samarium-153] EDTA for imaging of experimental tumor models. *J Nucl Med* 1989;30:202-8.
- [93] Yeong CH, Abdullah BJ, Ng KH, Chung LY, Goh KL, Sarji SA, et al. Production and first use of ¹⁵³SmCl₃-ion exchange resin capsule formulation for assessing gastrointestinal motility. *Appl Radiat Isot* 2012;70:450-5. Back to cited text no. 3

- [94] Marvola J, Kanerva H, Slot L, Lipponen M, Kekki T, Hietanen H, et al. Neutron activation-based gamma scintigraphy in pharmacoscintigraphic evaluation of an egalet constant-release drug delivery system. *Int J Pharm* 2004;281:3-10. Back to cited text no. 4
- [95] Wilding IR, Hardy JG, Sparrow RA, Davis SS, Daly PB, English JR, et al. In vivo evaluation of enteric-coated naproxen tablets using gamma scintigraphy. *Pharm Res* 1992;9:1436-41. Back to cited text no. 5
- [96] De Vries DJ, Moore S. Approximation of approximation of hexagonal holes by square holes in Monte Carlo simulation of gamma-camera collimation. *IEEE Trans Nucl Sci* 2002;49:2186-95.
- [97] Shafaei M, Ay MR, Sardari D, Dehestani N, Zaidi H. Monte Carlo assessment of geometric, scatter and septal penetration components in DST-XLi HEGP collimator. *IFMBE Proc* 2008;22:2479-82.
- [98] Ljungberg M, Larsson A, Johansson L. A new collimator simulation in SIMIND based on the delta scattering technique. *IEEE Trans Nucl Sci* 2005;52:1370-5.
- [99] Cot Sanz A, Pareto D, Sempau J, Bullich S, Pavia J, Calviño Tavares F, et al, Evaluation of the geometric, scatter, and septal penetration components in fan-beam collimators using Monte Carlo simulation. *IEEE Trans Nucl Sci* 2002;49:12-6.
- [100] Vandenberghe S, Van Holen R, De Beenhouwer J, Staelens S, Lemahieu I. Comparison of image quality of different iodine isotopes (I-123, I-124 and I-131). *Cancer Biother Radiopharm* 2007;22:423-30.
- [101] Autret D, Bitar A, Ferrer L, Lisbona A, Bardiès M. Monte Carlo modeling of gamma cameras for I-131 imaging in targeted radiotherapy. *Cancer Biother Radiopharm* 2005;20:77-84.
- [102] Pandey AK, Sharma SK, Karunanithi S, Kumar P, Bal C, Kumar R. Characterization of parallel-hole collimator using Monte Carlo simulation. *Indian J Nucl Med* 2015;30:128-34.
- [103] Simon R.Cherry, James A.Sorenson and Micheal E.Phelps , (2012):"Physics in nuclear medicine" .4th Edition, SAUNDERS Elsevier.
- [104] Bouzekraoui Y, Bentayeb F, Asmi H, Bonutti F. Comparison of image quality of different radionuclides technetium-99m, samarium-153, and iodine-123. *Indian J Nucl Med* 2019;34:201-4.
- [105] Bouzekraoui Y, Bentayeb F, Asmi H, Bonutti F. Energy window and contrast optimization for single-photon emission computed tomography bremsstrahlung imaging with yttrium-90. *Indian J Nucl Med* 2019;34:125-8.
- [106] Bouzekraoui Y, Bentayeb F, Asmi H, Bonutti F. Determination of Energy Windows for Triple Energy Window Scatter Correction Method in Gadolinium-159 Single Photon Emission Computed Tomography Using Monte Carlo Simulation. *Iran J Med Phys* 2019; 16:405-409.10.22038/ijmp.2019.34142.1429

- [107] Asmi H, Bentayeb F, Bouzekraoui Y, Bonutti F. Evaluation of acceptance angle in iodine-131 single photon emission computed tomography imaging with Monte Carlo simulation. *Indian J Nucl Med* 2019;34:24-6.
- [108] Asmi H, Bentayeb F, Bouzekraoui Y, Bonutti F. Energy window and collimator Optimization in Lu-177 SPECT imaging using Monte Carlo Simulation . *Indian J Nucl Med* 2020;35:36-9.

Résumé

Le choix du radionucléide a un rôle clé en médecine nucléaire qui apparaît comme la fraction de dispersion la plus faible. Le choix de la fenêtre d'énergie d'acquisition n'est pas trivial, du fait de la répartition énergétique continue et étendue des photons de Freinage. De plus, la présence de photons pénétrés et dispersés provenant du collimateur dans les images de tomographie par émission monophonique dégrade la résolution et le contraste. Ainsi, la qualité de l'image dépend de la sensibilité et de la résolution du système détecteur-collimateur. L'objectif de ce travail consistait tout d'abord à utiliser une étape différente du code de simulation SIMIND MC pour comparer la qualité d'image pouvant être obtenue avec trois radionucléides : technétium 99 m (Tc-99 m), iode 123 (I-123) et samarium. 153 (Sm-153), En imagerie de tomographie par émission monophotonique (SPECT) en yttrium 90 (Y-90), nous étudions les effets des fenêtres d'énergie sur le rapport de contraste de l'image sur l'image (CNR), afin de sélectionner la fenêtre d'énergie optimale pour l'imagerie Y 90. Et pour déterminer les fenêtres principale et secondaire d'énergie pour la méthode de correction de dispersion de fenêtre à triple énergie (TEW) à l'aide du code de simulation SIMIND Monte Carlo en imagerie Gadolinium-159 (Gd-159). Les résultats montrent que Tc-99m et Sm-153 donnent les meilleurs résultats, avec un collimateur LEHR pour la résolution spatiale, alors que, avec le collimateur ME, une résolution inférieure pour I-123, la fenêtre d'énergie optimale obtenue pour l'imagerie SPECT Y-90 bremsstrahlung (Freinage) était [120–150] keV, et les fenêtres d'énergie optimales pour la scintigraphie au Gd-159 étaient les fenêtres d'énergie secondaire de 3 et 6 keV. Ces résultats pourraient être utiles pour la quantification de l'imagerie Gd-159.

Mots-clés : Bremsstrahlung (Freinage), CNR, Fantôme Jaszczak, SIMIND, Imagerie par tomodensitométrie à émission de photons simples d'yttrium 90, rapports de diffusion au total, Sensibilité, Résolution spatiale.

Abstract

The choice of the radionuclide has a key role in nuclear medicine which appearing the lowest scatter fraction. the choice of the acquisition energy window is not trivial, due to the continuous and broad energy distribution of the bremsstrahlung photons. In addition, the presence of penetrated and scattered photons from collimator in single-photon emission computed tomography images degrade resolution and contrast. Thus, image quality depends on sensitivity and resolution of the collimator–detector system. The objective of this work was firstly how to use a different step of SIMIND MC Simulation Code, to compare the image quality that can be achieved by three radionuclides: technetium-99 m (Tc-99 m), iodine-123 (I-123), and samarium-153 (Sm-153), In yttrium-90 (Y-90) single-photon emission computed tomography (SPECT) imaging, we investigate the effects of the energy windows on the image contrast to noise ratio (CNR), in order to select the optimal energy window for Y-90 imaging. And to determine the main and sub-energy windows for triple energy window (TEW) scatter correction method using the SIMIND Monte Carlo simulation code in Gadolinium-159 (Gd-159) imaging. The results show that Tc-99 m and Sm-153 give best and results with LEHR collimator for spatial resolution, whereas, I-123 provided with ME collimator a lower resolution, also the optimal energy window obtained for Y-90 bremsstrahlung SPECT imaging was [120–150] keV, and the optimal energy windows for Gd-159 scintigraphy were the sub energy windows of 3 and 6 keV. These findings could be helpful in the quantification of Gd-159 imaging.

Keywords: Bremsstrahlung, CNR, Jaszczak phantom, SIMIND, yttrium-90 single-photon emission computed tomography imaging, Scatter to Total Ratios, sensitivity, spatial resolution,

Année Universitaire : 2019-2020